

Test beam performance of a CBC3-based mini-module for the Phase-2 CMS Outer Tracker before and after neutron irradiation

The Tracker Group of the CMS Collaboration

E-mail: uplegger@fnal.gov

ABSTRACT: The Large Hadron Collider (LHC) at CERN will undergo major upgrades to increase the instantaneous luminosity up to $5\text{--}7.5 \times 10^{34} \text{ cm}^{-2} \text{ s}^{-1}$. This High Luminosity upgrade of the LHC (HL-LHC) will deliver a total of $3000\text{--}4000 \text{ fb}^{-1}$ of proton-proton collisions at a center-of-mass energy of $13\text{--}14 \text{ TeV}$. To cope with these challenging environmental conditions, the strip tracker of the CMS experiment will be upgraded using modules with two closely-spaced silicon sensors to provide information to include tracking in the Level-1 trigger selection. This paper describes the performance, in a test beam experiment, of the first prototype module based on the final version of the CMS Binary Chip front-end ASIC before and after the module was irradiated with neutrons. Results demonstrate that the prototype module satisfies the requirements, providing efficient tracking information, after being irradiated with a total fluence comparable to the one expected through the lifetime of the experiment.

KEYWORDS: Particle tracking detectors (Solid-state detectors); Radiation-hard detectors

Contents

1	Introduction	2
2	The CBC3 front-end ASIC	3
3	The mini-module	5
4	Data acquisition system	6
5	Fermilab Test Beam Facility	8
6	Alignment and tracking	8
7	Neutron Irradiations at RINSC	10
8	Data sets	10
9	Module calibration	11
10	Detector setup	12
10.1	Latency optimization	12
10.2	Threshold optimization	14
10.3	Calibration of the rotation angle	15
11	Performance	16
11.1	Particle detection efficiency	16
11.1.1	Dependency on V_{CTH}	17
11.1.2	Dependency on the strip number	17
11.1.3	Dependency on relative position with respect to the center between adjacent strips	18
11.2	Pulse shape	18
11.3	Cluster width	20
11.4	Resolution	20
11.5	Charge collection	22
11.6	Stub reconstruction efficiency	24
12	Conclusions	28
	The Tracker Group of the CMS Collaboration	31

1 Introduction

The Large Hadron Collider (LHC) at CERN will undergo major upgrades to increase the instantaneous luminosity up to $5\text{--}7.5 \times 10^{34} \text{ cm}^{-2}\text{s}^{-1}$. This High Luminosity upgrade of the LHC (HL-LHC) [1] will provide an unprecedented sample of proton-proton collision data at a center-of-mass energy of 13–14 TeV, extending significantly the discovery potential of direct searches for new phenomena and the sensitivity of the precision measurement program. Compared to the LHC, the luminosity upgrade will increase the collision rates, detector occupancies, and the radiation induced damage. To cope with these challenging experimental conditions, the entire silicon tracking system of the CMS experiment [2] will be upgraded [3] with a new tracker, which will include an Inner Tracker based on silicon pixel modules and an Outer Tracker made from silicon modules with strip and macro-pixel sensors.

The new CMS Outer Tracker will be equipped with so-called p_T -modules, which consist of pairs of radiation-tolerant silicon sensors parallel to each other and separated by a few millimeters. This new design concept will enable CMS to include tracking information in the first level of the trigger (L1) selection. For the first time a selection on the transverse momentum of tracks can be used to select events of interest with high efficiency while maintaining trigger rates within the allowed bandwidth. Figure 1 illustrates the concept of operation of these p_T -modules. A hit in the bottom (seed) sensor opens a programmable search window in the top (correlated) sensor such that particles with momentum larger than 2–3 GeV should pass through this area while particles with lower momentum should not, due to their large curvature in the magnetic field. The seed sensor hit and the correlated sensor hit falling in the search window form a hit pair called stub which is used by the L1 trigger to decide whether the data for an event are to be read out.

Modules installed at radii from 20 to 60 cm from the beam line are named pixel-strip (PS) modules and consist of one strip sensor and one macro-pixel sensor, where macro refers to the unusual pixel size when compared to the Inner Tracker pixels, which for this sensor is $1.447 \text{ mm} \times 100 \mu\text{m}$. Modules at larger radii consist of two identical strip sensors and are named strip-strip (2S) modules. An exploded view drawing of the 2S module is shown in Fig. 2.

The PS modules are read out by the Macro Pixel ASIC (MPA [4]) and by the Short Strip ASIC (SSA [5]), while the 2S modules are read out by the CMS Binary Chip (CBC [6]). The MPA and CBC front-end ASICs have the logic implemented to correlate the hits in the seed and correlated sensors and create the stubs. The stub information is transmitted to the L1 trigger at the LHC collision frequency of 40 MHz, while the strip hit information is read out on receipt of a L1 trigger accept signal. Results from the characterization of a prototype 2S module based on the previous version of the CBC are discussed in Ref. [7], while this paper presents the performance of the first module based on a version of the CBC ASIC (CBC3) that incorporates the complete functionality, including the trigger logic. This module, featuring smaller sensors and built with only two CBC chips instead of the sixteen that equip a tracker module, is called mini-module.

Although the tracker will operate in the CMS magnetic field, all measurements presented in this paper were done in the absence of a magnetic field since no magnet was available at the Fermilab Test Beam Facility (FTBF).

This paper is organized as follows: Sec. 2 summarizes the main features of the CBC3 chip, Sec. 3 describes the mini-module and Sec. 4 discusses the mini-module data acquisition system (DAQ).

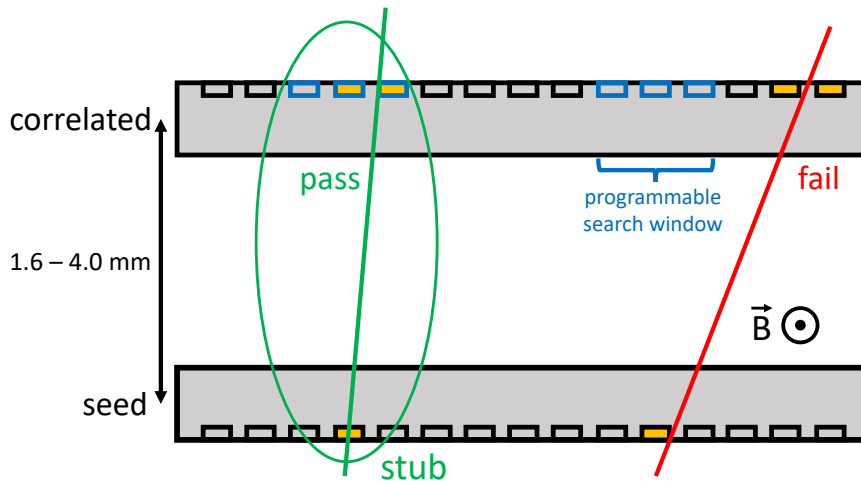


Figure 1: Illustration of the identification of particles with high transverse momentum. A hit in the bottom sensor opens a programmable search window in the top sensor such that particles with momentum larger than about 2–3 GeV should pass through this sensor area creating a stub, as pictured by the particle trajectory on the left. Particles with momentum smaller than 2–3 GeV will instead fail to go through the programmable search window not creating a stub, as pictured by the particle trajectory on the right.

The Fermilab Test Beam Facility is briefly described in Sec. 5 and the alignment and tracking software, in Sec. 6, while the Rhode Island Nuclear Science Center irradiation facility is described in Sec. 7. The collected data sets are summarized in Sec. 8. The final part of the paper presents the performance of the mini-module before and after irradiation, starting in Sec. 9 with the module calibration, followed by the steps to set up the necessary parameters to take data, Sec. 10. Finally, Sec. 11 presents the results of the module performance in the beam.

2 The CBC3 front-end ASIC

The CBC series is designed for the readout of the 2S modules of the Phase-2 CMS tracker. Manufactured in a 130 nm CMOS technology, the CBC chip reads out the charge produced via ionization by charged particles traversing the silicon sensors. The CBC converts the produced charge into a hit or no-hit binary value for each of the channels. Compared to earlier versions of the CBC [8], the CBC3, mounted on the mini-module, is the first version of the ASIC to include the full trigger logic circuitry for detecting potential high momentum tracks in each bunch crossing event.

Each CBC3 chip has 254 channels, each with a pre-amplifier, amplifier and the possibility to individually trim the effective threshold. The CBC3 operates with the 127 odd-numbered channels connected to the seed sensor and the 127 even-numbered channels connected to the correlated sensor of the module. One CBC3 ASIC then services 127 strips from each of two sensors.

The block diagram of the analog front-end of the CBC3 is shown in Fig. 3. Charge generated in the strip is read out by a pre-amplifier and integrated onto a 100 fF feedback capacitor. The feedback

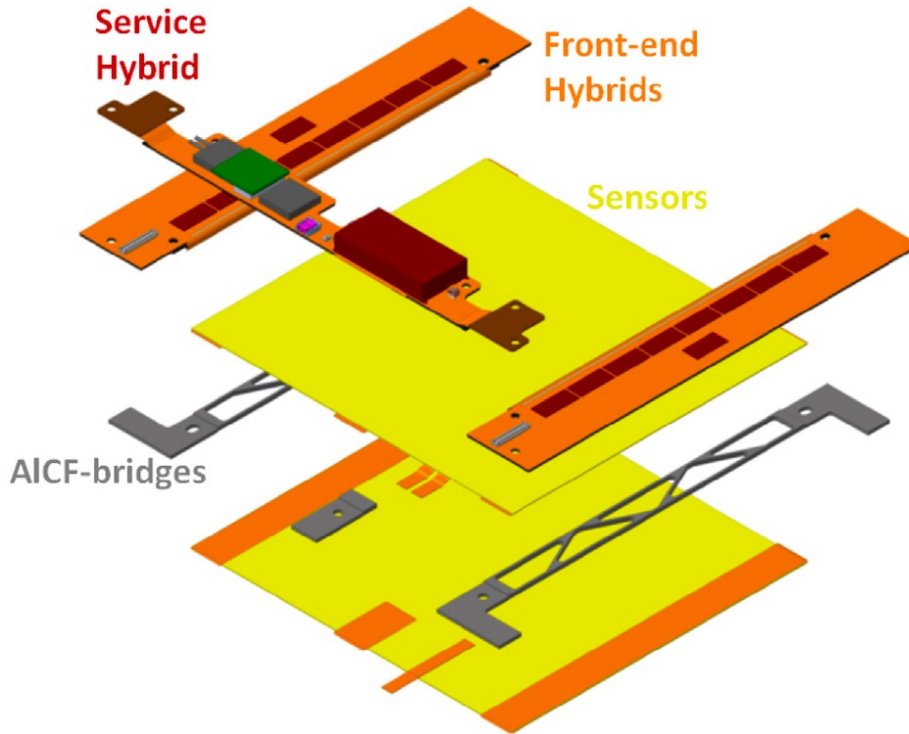


Figure 2: Exploded view of a 2S module. The seed and correlated sensors, in yellow, are separated by two aluminum carbon fiber bridges. The two front-end hybrids, in orange, are mounted on the two sides of the sensors. The service hybrid, in red, with two DC-DC converters inside an electromagnetic shielding box and the optical link to the DAQ, is mounted between the two front-end hybrids.

capacitor is discharged by a $100\text{ k}\Omega$ resistive feedback network. The resulting voltage pulse from the pre-amplifier is further amplified by a capacitive gain amplifier, which is stabilized by a large feedback resistance, V_{PAFB} . To compensate for any channel to channel threshold mismatch, due to the fabrication process, each amplifier has a programmable offset adjustment, named V_{PLUS} . These control currents are programmed via an 8-bit register in each channel, providing enough resolution to obtain a channel to channel variation of the average no-particle signal at the comparator input, called pedestal, of less than one hundred electrons. The comparator stage detects signals which cross a defined adjustable global chip threshold, V_{CTH} , and will produce a digital 1 output for as long as the signal stays above the threshold. The various analog biases used by the front-end circuits are derived on-chip, from the analog voltage V_{DDA} , using bias generation circuits powered by a voltage reference band gap. The band gap circuit uses a PMOS transistor in place of the more traditional diode, which makes it more tolerant to radiation damage, but leaves it susceptible to process variation.

AC coupled n-in-p type silicon sensors were chosen for the tracker, so the CBC3 channel will operate for the readout of electrons. Since the AC coupling circuit is included in the sensor, there is no leakage current compensation circuit included in the CBC3 design. Each input is bonded to one strip of a silicon sensor.

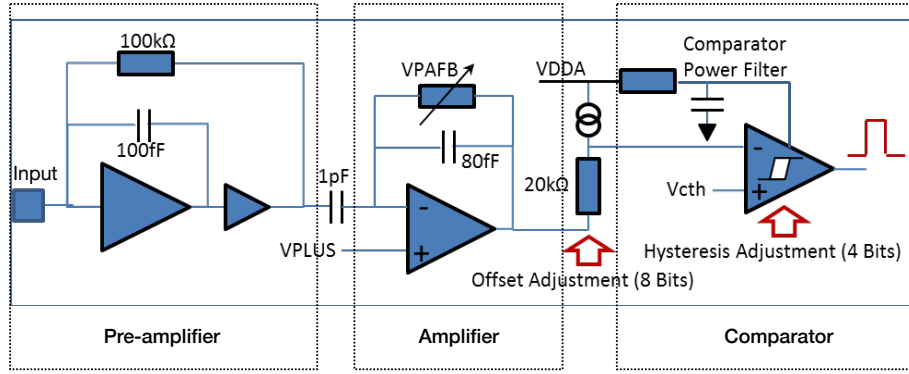


Figure 3: Block diagram of the analog front-end of the CBC3 ASIC.

3 The mini-module

The prototype p_T -module was assembled at CERN and consists of two sensors produced by Infineon [9]. The two identical AC coupled strip sensors are made from high resistive float zone silicon, thinned to a physical and active thickness of $300\ \mu\text{m}$. The 254 strips per sensor use polysilicon bias resistors and p-stop strip isolation and are approximately 5 cm long with a pitch of $90\ \mu\text{m}$ and a width-to-pitch ratio of 0.25 [10]. The strip geometry is close to the final 2S sensors and therefore also the capacitance seen by the readout chip. The sensors are mounted on an aluminum structure to keep them separated by $d = 1.8\ \text{mm}$ (where d is the distance between the mid-planes of the sensors). A prototype hybrid [11] with two CBC3 front-end ASICs is wire-bonded to the sensors and read out through an interface board (Universal Interface Board, or UIB). The CBC3 ASICs mounted on this hybrid are both version 3.0, while the final version of the chip that will be used in the detector is version 3.1. The assembly is referred to as mini-module in the rest of the paper.

A dedicated structure was designed and manufactured to support and cool the mini-module. As shown in Fig. 4 (a), the cooling liquid flows through the pipes embedded in the cooling plate, and a temperature sensor is installed on the cooling plate itself. An aluminum support hosts the mini-module and is mounted on top of Peltier elements, used to help regulate the temperature, and in turn is cooled down by the cooling plate. All plates have a rectangular hole to allow the beam to pass through to minimize multiple scattering. The support structure and the mini-module are installed in a 3D-printed enclosure that is flushed with dry air to prevent condensation. The enclosure, with foam used as insulation between the cooling plate and the plastic, is wrapped with copper tape to ensure electromagnetic shielding and to avoid penetration of light. The UIB is installed outside the enclosure and connects to the back-end DAQ board, called FC7 [12], via a very high density cable interconnect (VHDCI). The final assembly is shown in Fig. 4 (b).

The default running configuration for the mini-module is the following, unless specified otherwise:

- unirradiated: $V_{\text{bias}} = -300\ \text{V}$; temperature = $+15\ ^\circ\text{C}$; $V_{\text{CTH}} = 560\ \text{DAC units}$;
- irradiated: $V_{\text{bias}} = -600\ \text{V}$; temperature = $-20\ ^\circ\text{C}$; $V_{\text{CTH}} = 540\ \text{DAC units}$.

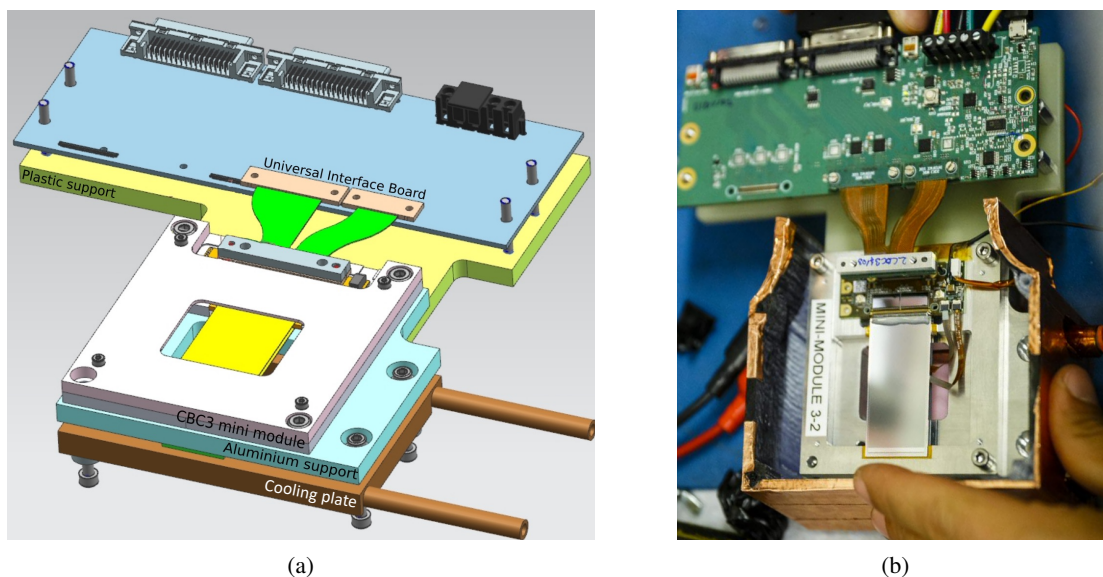


Figure 4: (a) Drawing of the mini-module support structure. (b) Mini-module mounted on the support structure, hosted in the enclosure, and connected to the UIB.

4 Data acquisition system

The data acquisition system used to read out the mini-module is based on the CMS-specific custom μ TCA FC7 back-end board which is electrically connected to the CBC3 chips on the hybrid circuit. A sketch of the DAQ connections is shown in Fig. 5. Both CBC3 chips are connected to a common control interface consisting of a 320 MHz clock line, two lines for communication with the chips via the I2C protocol, a dedicated reset line, and a fast-command line on which 8-bit synchronous commands are transmitted. The signals that can be encoded on this line are a fast-reset, a trigger signal, a request for a test pulse, and a reset to zero of the on-chip trigger counter. Data from the chips are sent on six sub low voltage differential signaling (SLVDS) lines. Five of these lines are reserved for the stub data, which are sent bunch-synchronous at 40 MHz to be used in the L1 trigger decision. The sixth line is reserved for hit data, which are only sent on reception of a trigger signal.

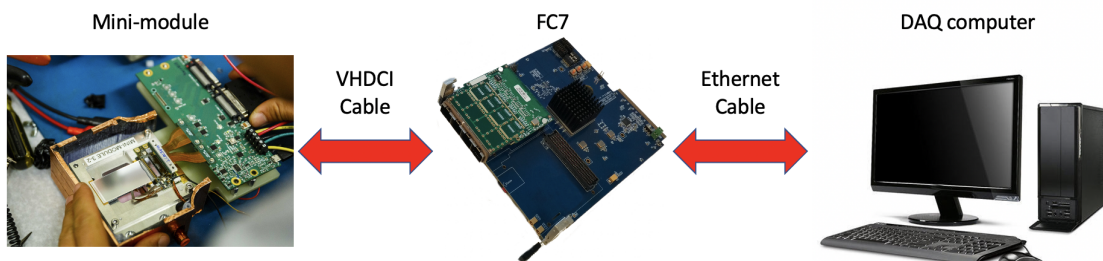


Figure 5: Data acquisition schematic view. The mini-module is connected to the FC7 back-end board through a VHDCI. The FC7 is then connected to the DAQ computer with an ethernet cable.

Since the SLVDS drivers on the CBC3 chip can only drive these signals over a very short distance, the UIB is used to interface the chips to the back-end electronics. It is connected to the hybrid via a short, flexible jumper cable and has a number of SLVDS level translators to drive the signals to the readout card over the 1 m long VHDCI. In addition, the UIB provides the low voltage power for the hybrid circuit and has an integrated ADC to monitor the hybrid power consumption and temperature.

The CMS-specific FC7 card is the basis of the readout system developed for the prototyping phase of the CMS Outer Tracker. It has a Xilinx Kintex 7 FPGA and is equipped with two high-pin-count FPGA mezzanine card (FMC) connectors to adapt the FC7 to a variety of applications. The VHDCI from the UIB is connected to a custom-built mezzanine card, sitting on one of the FMC connectors, that routes the differential signals to the FPGA for processing. For this test beam, a second dedicated FMC was used to interface the FC7 to the triggering system used at the Fermilab Test Beam Facility. Through this second FMC board, the system clock and the trigger signal from the scintillator coincidence were connected to two differential inputs on the FPGA. A differential output was used to send a busy signal to the trigger control logic to inhibit further triggers in case of imminent buffer overflow.

The custom firmware running on the FC7 is controlled by a common software framework written in C++ called Phase-2 Acquisition and Control Framework (Ph2-ACF). This framework has been developed to cover all R&D and testing needs during the prototyping phase for the Phase-2 Tracker of CMS. It is based on the μ HAL/IPBUS [13] libraries that allow for simple, yet reliable write/read operations of firmware registers based on the TCP/IP protocol. The core feature of the Ph2-ACF framework is that it introduces an abstraction layer between the μ HAL calls and the higher-level user code. This allows full control over CBC functionalities such as configuring the chips via the I2C registers, sending fast commands, and reading out data, without further knowledge of the firmware structure. Furthermore, utilities for event data decoding and data storage are provided within the framework.

The CBC chips are reset and configured before each run. The flow of triggers is enabled as soon as the system is ready. The main thread of the Ph2-ACF then runs a polling loop that continuously queries the state of the "data-ready" flag in the FC7 firmware. Once the firmware signals that data are available to be read out, the main thread performs a block-read operation of the data FIFO. This data block is shared with various consumer threads that store the binary raw data directly on disk without further processing. Consumer threads also decode the data into individual events for processing and re-formatting into the final 64-bit CMS SLINK data format.

A supervisor application based on the CMS XDAQ framework [14] has been developed around the Ph2-ACF libraries to allow straightforward integration into the FTBF tracking telescope DAQ based on the OTSDAQ framework developed by the Fermilab Computing Division [15], described in Sec. 5. This application provides all the interfaces required to communicate with the run control system and implements a finite state machine that ensures synchronicity of all elements of the DAQ system. In addition, it offers a browser-based graphical user interface that allows to easily edit configurations and monitor the status of the system.

Data quality monitoring is provided by a simple application, also based on the Ph2-ACF libraries, that runs asynchronously on the SLINK files once they are written to disk. This application provides basic histograms to monitor the recorded data within a very short turnaround time, which allows

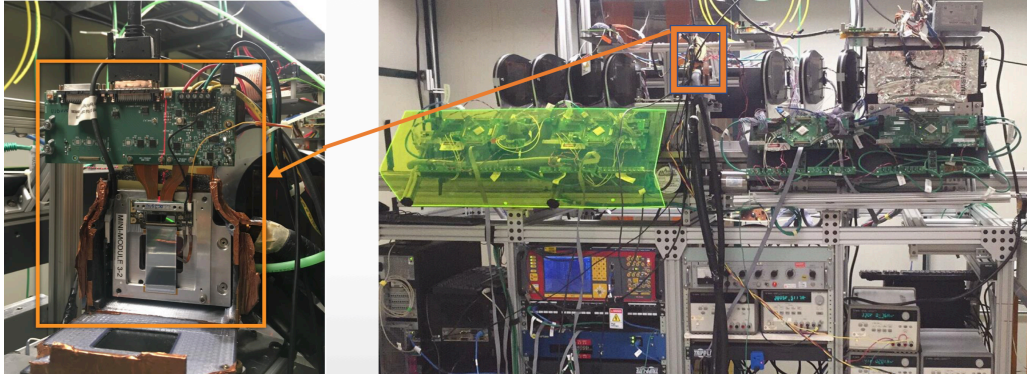


Figure 6: FTBF silicon telescope. The mini-module is installed in the middle.

issues with the system to be detected immediately.

5 Fermilab Test Beam Facility

The mini-module was tested at the Fermilab Test Beam Facility [16], which provides a 120 GeV bunched proton beam at rates ranging from 1 to 300 kHz. The beam is delivered to the facility every minute with the spill lasting 4 seconds. The test beam campaign described in this paper used the 120 GeV proton beam at rates between 20 and 50 kHz.

Figure 6 shows the tracking telescope available at the FTBF and the mounting position of the mini-module. The mini-module was mounted on a remotely controlled rotation platform provided by the FTBF. The facility does not have a magnet so all tests were performed in the absence of a magnetic field. A chiller, necessary to keep the irradiated device cold to minimize the sensors' annealing, was already present at FTBF and used during the tests. The telescope, which provides precision tracking information, consists of four planes equipped with pixel modules, placed downstream, and fourteen planes equipped with strip modules [17], placed before and after the detector under test. The pixel modules are identical to those used for the Phase-0 CMS Forward Pixel detector and are based on the PSI46 front-end chip [18]. Two of the pixel layers are equipped with 2×3 modules, and the other two layers with 2×4 modules, where 2×3 and 2×4 refer to the number of PSI46 chips present in the module. The strip sensors were designed for the Run 2b upgrade of the D0 tracker [19] and are read out by the FSSR2 front-end chip [20]. The telescope resolution, measured at the position where the mini-module was mounted, was approximately $7 \mu\text{m}$.

Two scintillator counters provided the coincidence signal from the particles in the beam. A Fermilab-designed FPGA-based trigger board synchronized the data streams of the telescope and the mini-module. This trigger board accepts the scintillator counters' NIM signals and it also generates a 39.75 MHz clock, multiplying the 53 MHz Fermilab accelerator clock by $\frac{3}{4}$, thus keeping the beam and clock phases fixed relative to each other.

6 Alignment and tracking

The track reconstruction and the telescope alignment are performed by means of a dedicated package called Monicelli [17]. This software provides the user with an iterative procedure to converge

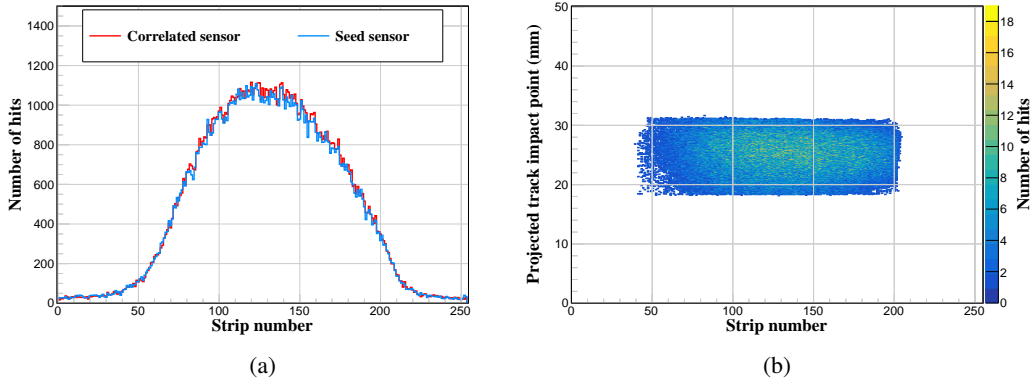


Figure 7: (a) Distribution of hits for the seed and correlated sensors of the unirradiated mini-module. (b) 2D hit map where the x -axis represents the strip number and the y -axis the projected track impact point along the strip direction.

toward the optimal alignment of the telescope. All operations can be accomplished in steps through a graphical interface that makes the software user-friendly. The track-reconstruction code implemented in Monicelli is a generic alignment program developed for the FTBF telescope. It performs a Kalman filter fit to the coordinates of the arrays of hits, which were preselected by pattern recognition based on their proximity, $\pm 500 \mu\text{m}$, to a straight line connecting a hit on the first plane and a hit on the last plane of the telescope. In the case of clusters of adjacent pixels or strips, the hit coordinates are calculated exploiting the linear relationship between the relative amount of charge shared by the two pixels or strips in the cluster and the proximity of the hit to the boundary between them. The linear relationship was measured during the first commissioning phase of the telescope. The errors attributed to the coordinates were also calibrated during the telescope commissioning. To perform this track reconstruction process, Monicelli reads a binary file containing the telescope and mini-module merged events together with an XML geometry file describing the overall configuration and geometrical details of the telescope detectors for that particular data set. The Monicelli software output file consists of a ROOT TTree [21] containing, for each event, the reconstructed telescope tracks together with the associated clusters of hits and the raw data, including those of the mini-module. This output file provides the user with all the information needed for the analysis of the test beam data.

Figure 7 (a) shows an example of a hit distribution for the seed and correlated sensors of the unirradiated mini-module, placed orthogonally to the incident beam. A 2D hit map, shown in Fig. 7 (b), can be reconstructed using the strip number as one coordinate, with the position along the strip direction obtained by interpolating the reconstructed telescope track to the mini-module position. The 2D map does not extend over the whole sensor due to the telescope acceptance and the beam size.

7 Neutron Irradiations at RINSC

The Rhode Island Nuclear Science Center (RINSC) operates a 2 MW light-water cooled, open pool type reactor on the Narragansett Bay Campus of the University of Rhode Island, USA. The core consists of fuel assemblies and a combination of graphite and beryllium reflectors. The fuel is plate type U_3Si_2 clad with aluminum, enriched to less than 20% Uranium-235. The reactor provides several ways to irradiate samples, among others a pneumatic rabbit system that is suitable for small samples and beam ports that can accommodate larger samples. The mini module was irradiated in a 6-inch beam port, which is a pipe of 6 inch inner diameter that allows samples to be inserted close to the reactor core. An acrylic cylinder with a diameter just under 6 inches and a length of 2.5 feet was used to hold the mini-module with enough padding to protect it from physical damage. Ultra-pure foils and silicon diodes for dosimetry and two probes to monitor the temperature of the module during irradiation were packaged with the mini-module. During irradiation, samples get heated up by the gamma radiation in the reactor. To limit the heating and the resulting annealing of the silicon sensors the remaining volume of the cylinder was filled with dry ice. The module was irradiated for 16 minutes two separate times. The reactor has to be off for the module to be loaded into the beam port. It then is ramped up to 100% power and ramped down again after the desired irradiation time so that the module can be removed from the beam port. This procedure introduces significant edge effects that make it difficult to achieve a very precise irradiation time. The two irradiations resulted in fluences of 2.0×10^{14} and 2.4×10^{14} n_{eq}/cm^2 , where n_{eq} stands for 1-MeV-equivalent neutrons. The maximum temperature measured in the cylinder during irradiation was +30 °C.

8 Data sets

The mini-module was tested during three different test beam campaigns at the FTBF. The first run was done in November 2017 to assess the mini-module functionality and performance after assembly. After this run, the mini-module was irradiated with neutrons at the RINSC reactor. The main goal of the irradiation was to test the radiation tolerance of the sensors and to evaluate the overall performance of the mini-module assembly to make sure that the CBC3 would work as expected when connected to sensors with higher leakage current. The CBC3 chip radiation tolerance was previously studied using X-rays at CERN [22], since ionizing radiation is the main source of radiation damage for integrated circuits, and it demonstrated that the chip is capable of withstanding the levels of radiation expected at the HL-LHC with minimal degradation.

The accumulated fluence during this first irradiation was 2.0×10^{14} n_{eq}/cm^2 . The mini-module was then tested again in June 2018 at Fermilab. During this second test beam campaign, due to a problem with the cooling system, the mini-module was kept at +60 °C for two hours, effectively annealing part of the sensor damage due to the neutron irradiation. This annealing time can be converted into an equivalent annealing time at +21 °C, which is the temperature at which the detector is supposed to be annealed during maintenance periods in CMS, using the current-related damage rate at different temperatures. The conversion factor is calculated according to the parametrization given in Ref. [23] and the equivalent time at +21 °C is 20 days. The future tracker is expected to spend 20 weeks at that temperature in CMS, corresponding to two weeks of maintenance every year for at least 10 years. After the second test beam campaign, the mini-module was irradiated a

second time at RINSC and received an additional fluence of $2.4 \times 10^{14} \text{ n}_{\text{eq}}/\text{cm}^2$, resulting in a total accumulated fluence of $4.4 \times 10^{14} \text{ n}_{\text{eq}}/\text{cm}^2$. This total accumulated fluence exceeds the maximum fluence of $4.0 \times 10^{14} \text{ n}_{\text{eq}}/\text{cm}^2$ after 4000 fb^{-1} expected for more than 95% of the 2S modules in CMS [24]. After this last irradiation, the mini-module was tested at the FTBF for the third time in December 2018. The test beam campaigns and relative fluences are summarized in Table 1.

Table 1: Data set summary.

Test beam period	Total fluence ($\text{n}_{\text{eq}}/\text{cm}^2$)	Label
November 2017	0	Unirradiated
June 2018	2.0×10^{14}	Half fluence
December 2018	4.4×10^{14}	Full fluence

9 Module calibration

As mentioned in Sec. 2, the CBC3 may exhibit channel-to-channel variation of the pedestals with respect to the comparator threshold due to fabrication tolerances. To ensure a uniform distribution of pedestals across one chip, the calibration procedure (referred to as "pedestal and noise calibration" and described below) equalizes the distance of the pedestals from the comparator threshold, which is set globally by a register of the CBC3 (V_{CTH} in Fig. 3). A uniform distribution of pedestals results in the lowest possible common threshold (Sec. 10.2). The pedestal and noise calibration is performed in two steps. The first step is a scan of the V_{CTH} register, starting from high threshold values, until the number of hits, or module occupancy, reaches 50% of the number of triggers. The V_{CTH} value at which the occupancy is 50% is the chip average pedestal value. After the initial determination of the pedestal, each individual channel is then calibrated changing its programmable offset (V_{PLUS} in Fig. 3) until the channel occupancy reaches 50%. This individual channel pedestal shift is accomplished by adjusting the current through the $20 \text{ k}\Omega$ resistor shown in Fig. 3.

The V_{PLUS} values, calibrated during this first step of the procedure, are then saved and used for the second step to obtain the pedestal and noise distributions from the individual channel S-curves. An S-curve is obtained by sweeping V_{CTH} and measuring the occupancy for a fixed number of triggers. The final pedestal value and the channel noise are extracted differentiating numerically the S-curve and then calculating the mean and the σ of the obtained distribution. The mean corresponds to the pedestal value and the σ corresponds to the noise. An example of an S-curve recorded on a CBC3 is shown in Fig. 8, where higher numerical values of V_{CTH} correspond to lower thresholds in the CBC3.

Figure 9 shows the uniformity of the front-end response and the noise after the pedestal and noise calibration at two temperatures, $+15 \text{ }^\circ\text{C}$ and $-20 \text{ }^\circ\text{C}$. With the sensor biased to full depletion, which for this sensor is above 280 V , the channel-to-channel variation of the module pedestal is 139 and 86 electrons at $+15 \text{ }^\circ\text{C}$ and $-20 \text{ }^\circ\text{C}$, respectively. The conversion between DAC units and electrons is measured using an external X-ray source to be 156 electrons per V_{CTH} DAC unit and it does not depend on temperature. The average pedestal position changes between different temperatures by 19 DAC units, from 587 at $+15 \text{ }^\circ\text{C}$ to 568 at $-20 \text{ }^\circ\text{C}$. The noise mean value is 890 electrons when it

is measured at $+15^\circ\text{C}$ and decreases to 765 electrons at -20°C .

The pedestal and noise were measured again at -20°C after the different irradiation campaigns and the results are shown in Fig. 10. The positions of the pedestal distributions (in DAC units) do not shift significantly with irradiation, but the distribution broadens after the full fluence has been delivered. The noise distribution does not change significantly when the detector is half irradiated, but broadens upwards after the full irradiation. Using the same X-ray calibration as above it is possible to convert the V_{CTH} register into electron units. For example, for the default V_{CTH} value of 560 at $+15^\circ\text{C}$, with the pedestal at 587, the corresponding threshold in electrons is about 4200. A very similar value in electrons is calculated for the default V_{CTH} value of 540 at -20°C , since also the pedestal shifts by 19 DAC units.

10 Detector setup

10.1 Latency optimization

For every clock cycle, each individual binary strip hit is stored into a pipeline SRAM in the CBC3. Upon reception of a trigger, the corresponding data are sent to the DAQ back-end. If the particle is detected at t_0 and the trigger, associated to that particle, is received by the CBC3 at t_1 , then $L_{\text{data}}=t_1 - t_0$ represents the data latency that the CBC3 chip must take into account when it associates a particular event stored in the SRAM at t_0 with the trigger received at t_1 . A similar latency needs to be defined for the stubs which, as soon as a particle is detected and a stub is formed, are sent to the DAQ back-end where they are stored in the RAM in the FPGA. For the stubs, t_0 is defined as the time when the stub data are stored in the FPGA, while t_1 is the time when the trigger, associated with those stubs, is received by the FPGA. Similarly to L_{data} , L_{stub} is defined as the time that the FPGA needs to take into account when it associates stubs to their corresponding trigger. The latencies are measured in units of 40 MHz clock cycles and while L_{data} is set using an on-chip configuration register, L_{stub} is instead set using a register in the back-end FPGA. Both latencies were specific to the trigger system used during the test beam and they both needed to be measured before taking any meaningful data. The procedure to measure the two latencies is the same and relies on the fact that the beam particles, at the FTBF, are separated by many clock cycles. To determine the latency, 1000 triggers per latency setting were used. The

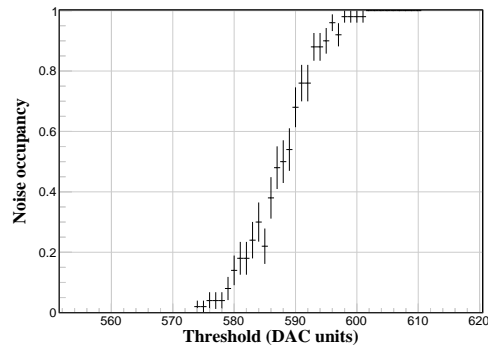


Figure 8: Single channel S-curve for the unirradiated mini-module.

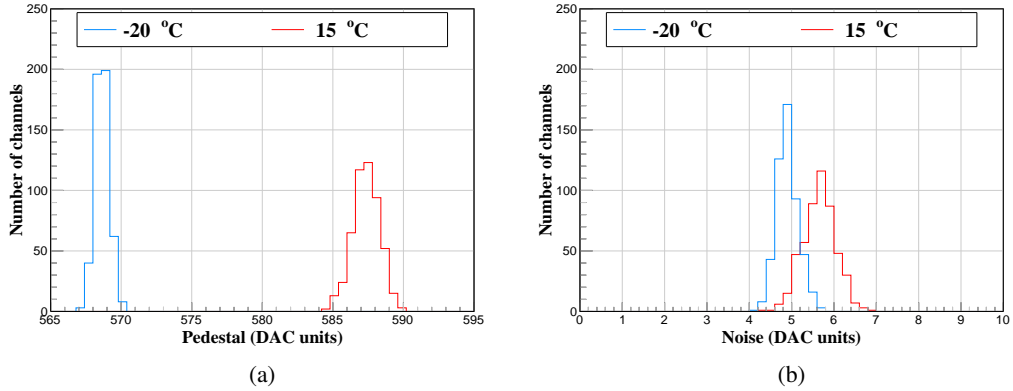


Figure 9: (a) Pedestal and (b) noise distributions for the unirradiated mini-module.

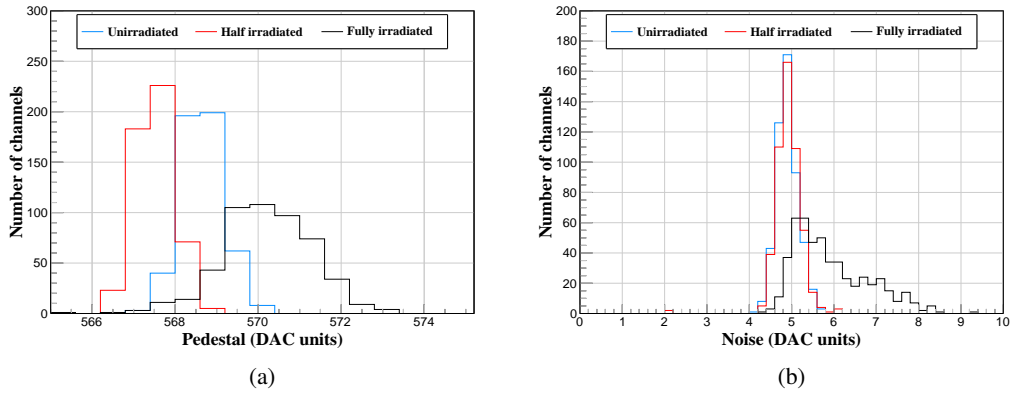


Figure 10: (a) Pedestal and (b) noise distributions for different irradiation fluences at -20°C .

correct values of the data and stub latencies are the ones that maximize the particle detection and stub efficiencies, respectively, as shown in Fig. 11. The details regarding the determination of the particle detection and stub efficiencies are provided in Sec. 11.1. Two more steps are necessary to tune the relative phase of the CBC3 clock and the beam. The beam synchronization with the CBC3 clock is done using the trigger board as described in Sec. 5. This optimization is done using a high resolution time-to-digital converter (TDC) implemented in the trigger board FPGA. The TDC is a 3 bit counter (0-7) operating at 320 MHz, and can thus shift the clock delivered to the back-end board and used by the mini-module by 3.125 ns. The procedure to optimize the TDC phase is done changing the counter every 1000 triggers and measuring, for each value of the counter, the particle detection efficiency. The TDC scan for the unirradiated mini-module is shown in Fig. 12 (a). The value of the TDC phase used during data taking is the one which maximizes the particle detection efficiency and it is the farthest away in time from the phases where the efficiency is dropping. From Fig. 12 the TDC operating value chosen was 0. The relative phase is further optimized scanning the CBC3 internal DLL register, which has a time resolution of 1 ns (Fig. 12 (b)). The optimization of the DLL is done changing the register every 1000 triggers and counting, for each latency and

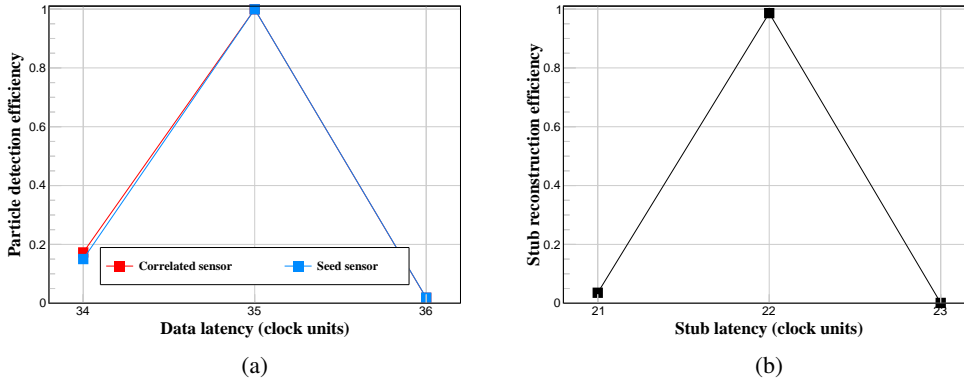


Figure 11: (a) Particle detection efficiency for each sensor at different values of the data latency. (b) Stub reconstruction efficiency at different values of the stub latency. The latencies are measured in units of 40 MHz clock cycles. Results are shown for the unirradiated module.

for every register value, the number of hits recorded on the mini-module. The optimal DLL setting was determined to be the one just before the number of hits were increasing for latency 36 and decreasing for latency 35. Figure 12 (b) shows that this condition was met between 2 and 3 ns. The DLL operating value chosen was 1.

10.2 Threshold optimization

The optimal comparator threshold is defined as the threshold that maximizes the particle detection efficiency and maintains the noise hit occupancy, defined as the probability of recording a noise hit in a channel per bunch crossing, below 10^{-4} . The optimal V_{CTH} value was determined to be 560 DAC units by measuring the particle detection efficiency and the number of clusters as a function of

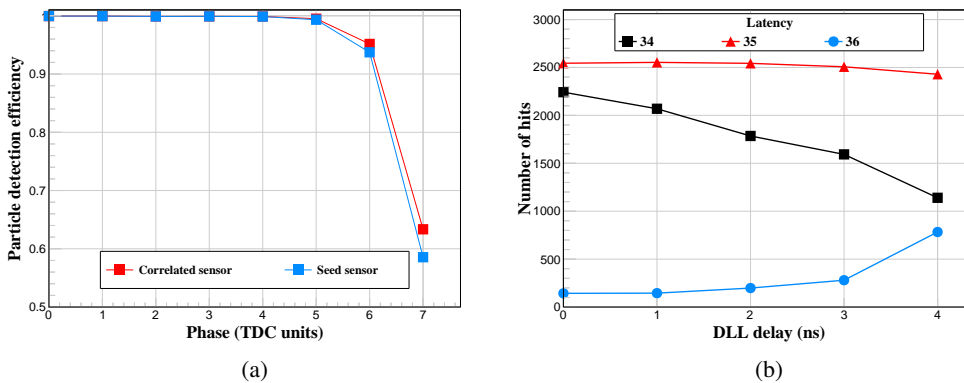


Figure 12: (a) Particle detection efficiency as a function of the TDC phase, in units of 3.125 ns for the seed and correlated sensors of the unirradiated mini-module. (b) Number of hits as a function of the DLL delay for three different latencies.

the threshold. The number of clusters increases substantially, due to noise, only when the threshold is close to the pedestal, as shown in Fig. 13 for the unirradiated mini-module. Figure 14 shows the efficiency and the noise hit occupancy as a function of V_{CTH} for the unirradiated, half irradiated, and fully irradiated mini-module and indicates that a threshold of 4200 electrons is optimal in all cases. Figure 14 also shows that in all runs the threshold could be lowered to values that kept the particle detection efficiency well above 99%. In particular, for the fully irradiated mini-module, where the efficiencies start dropping earlier due to the reduced amount of charge collected, it is possible to achieve high efficiencies with a noise level below 10^{-4} .

10.3 Calibration of the rotation angle

The last step in the setup procedure was to determine the offset in the rotation angle between the mini-module and the beam. The mini-module was mounted on a rotation stage with the strips pointing in the vertical direction. The module was rotated around the vertical axis. The angle of the mini-module could be changed in steps of half a degree using the rotation stage. Information about the alignment is extracted from the measurement of the impact point difference between the two mini-module sensors, which is shown in Fig. 15. The stub displacement ΔX can be written as

$$\Delta X = \Delta X_0 + \frac{d}{p} \tan(\beta_{\text{rot}} + \beta_0), \quad (10.1)$$

where β_{rot} is the angle as read off from the rotation stage, β_0 the angular offset between the beam and the normal to the mini-module at $\beta_{\text{rot}} = 0$, $d = 1.8 \text{ mm}$ the distance between the two sensors, $p = 90 \mu\text{m}$ the strip pitch, and ΔX_0 the translational misalignment of the two sensors. Using eq. 10.1, it is possible to fit the data, as shown in Fig. 15 and measure β_0 or, equivalently, ΔX_0 at $\beta_{\text{rot}} = 0$. Fixing $\Delta X_0 = 0$, the fit returns the angular misalignment $\beta_0 = 0.385^\circ \pm 0.004^\circ$, that is needed to correct the beam incident angle. A similar analysis has been done for each data set and the measured misalignment values have been used to correct the beam incident angle for each run. All plots and results presented in this paper have these corrections applied.

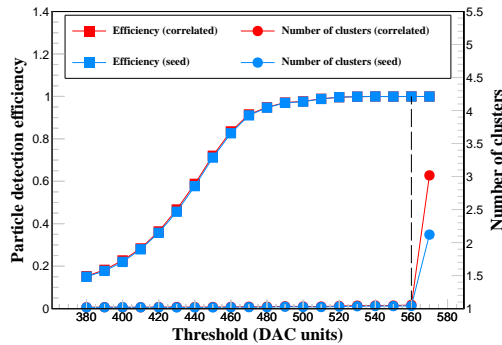


Figure 13: Particle detection efficiency and number of clusters detected per event as a function of V_{CTH} , for the unirradiated mini-module. The dashed line corresponds to the optimal threshold.

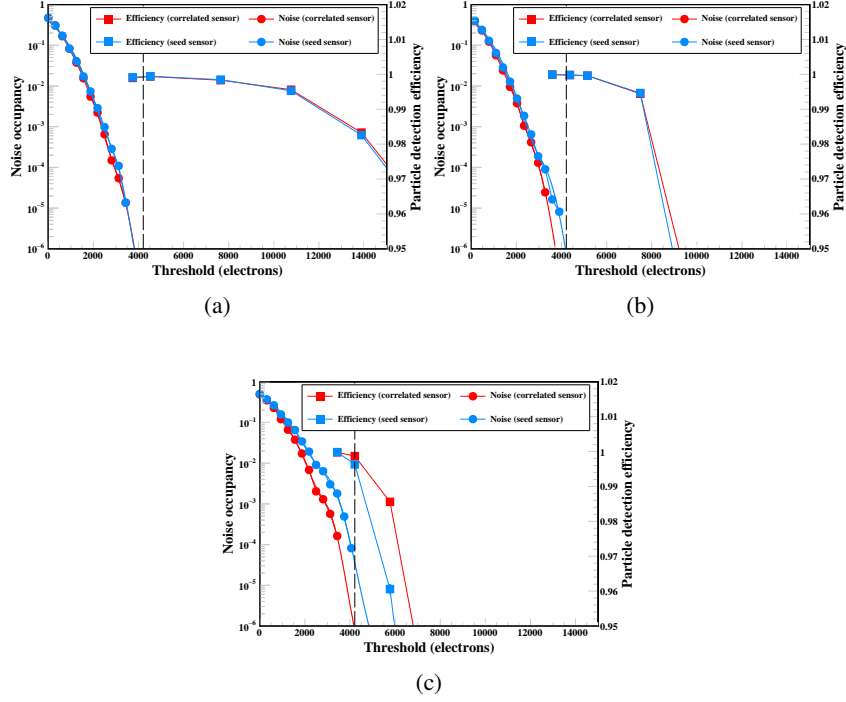


Figure 14: Particle detection efficiency and noise occupancy as a function of V_{CTH} for the unirradiated (a), half irradiated (b), and fully irradiated (c) mini-module. The dashed lines correspond to the optimal threshold.

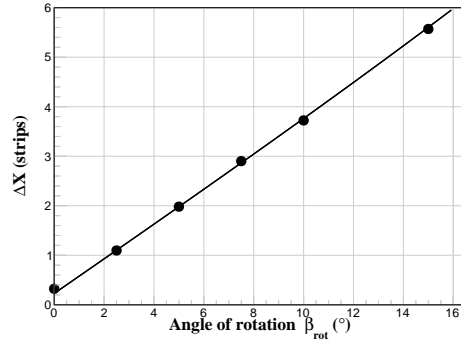


Figure 15: Mean stub displacement measured for different angles of the mini-module.

11 Performance

11.1 Particle detection efficiency

To measure the particle detection efficiency, tracks were selected with the following criteria:

- a track must traverse all telescope planes or miss at most one;
- there cannot be more than two clusters on any telescope plane;

- there can only be one reconstructed track;
- the track must have a $\chi^2/\text{ndof} < 5$.

These stringent criteria lead to a high quality data set. Inefficiencies due to edge effects were avoided by excluding cases where the predicted track pointed to a masked region or outside the active area of the sensor under study. The above criteria defined the sample of events for the measurement (with size N_{tot}). The particle detection efficiency is then measured as the number of events where the projected track is matched to a cluster within a window of $\pm 135 \mu\text{m}$ divided by N_{tot} . In what follows, the efficiency is presented as a function of V_{CTH} , the strip number, and the relative position of the track with respect to the center of the strip.

11.1.1 Dependency on V_{CTH}

Efficiency scans were performed to measure the impact of irradiation on the mini-module's performance. Figure 16 compares the efficiency measured in three threshold scans corresponding to the different irradiation conditions. The mini-module is more than 99.5% efficient for thresholds as high as 7000 electrons when unirradiated and half irradiated, far beyond the standard working threshold of 4200 electrons. After the full irradiation, the mini-module is still more than 99% efficient at a threshold of 4200 electrons, but the efficiency starts dropping rapidly for values above 5000 electrons. These scans thus show that the module works efficiently at thresholds lower than 5000 electrons even when the charge collected is reduced by irradiation, see Sec. 11.5.

11.1.2 Dependency on the strip number

Figure 17 shows that the efficiency as a function of the strip number for the unirradiated mini-module is close to 100%, while for the fully irradiated mini-module the efficiency is slightly reduced but it still exceeds 98.5% everywhere. In both cases the threshold was set to the standard value of 4200 electrons. The particle detection efficiency has a very large statistical uncertainty at the edges of the narrow beam which is mostly hitting the center of the sensors.

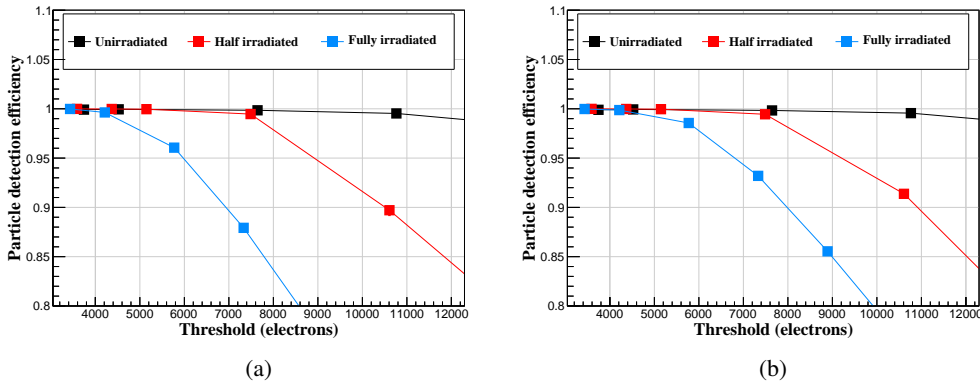


Figure 16: Particle detection efficiency vs. V_{CTH} for the different irradiation fluences. (a) Seed sensor, (b) correlated sensor.

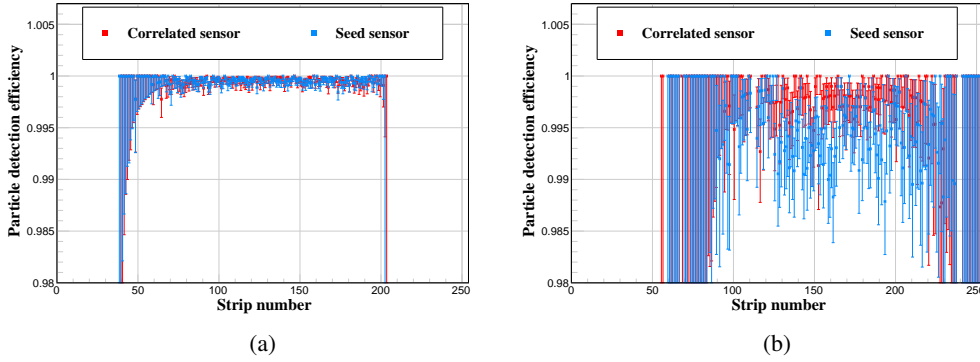


Figure 17: Particle detection efficiency along the sensor for the unirradiated (a) and the fully irradiated (b) mini-module.

11.1.3 Dependency on relative position with respect to the center between adjacent strips

The particle detection efficiency was also measured as a function of the relative position of the track to the center between adjacent strips to check for possible inefficiencies due to the reduced amount of charge collected by individual strips when the charge is shared. The study was performed for different thresholds, Fig. 18 (a), and for the different irradiation configurations, Fig. 18 (b). The results indicate that, due to charge sharing, there is a small inefficiency only at very high thresholds or when the mini-module is fully irradiated.

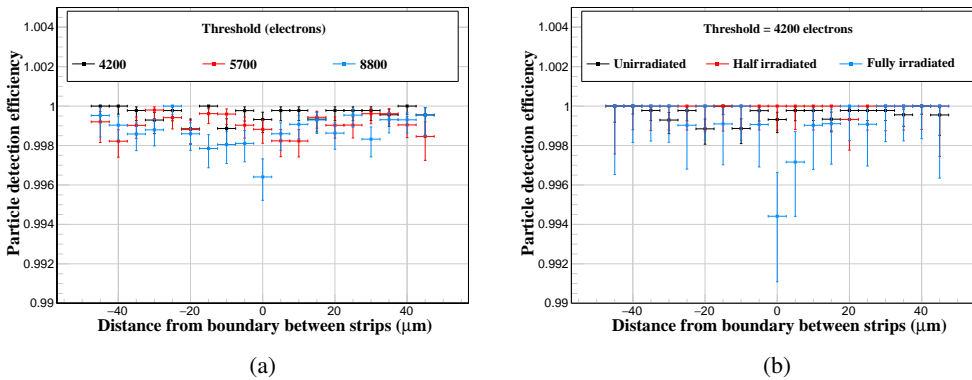


Figure 18: Particle detection efficiency as a function of the track location with respect to the center between adjacent strips for different thresholds of the unirradiated mini-module (a) and for different irradiation fluences (b).

11.2 Pulse shape

A measurement of the CBC3 amplifier pulse shape and peaking time has been performed during the final test beam campaign when the mini-module was fully irradiated to verify that the chip continues to meet the requirement of a peaking time around 20 ns and a return to baseline within 50 ns. This

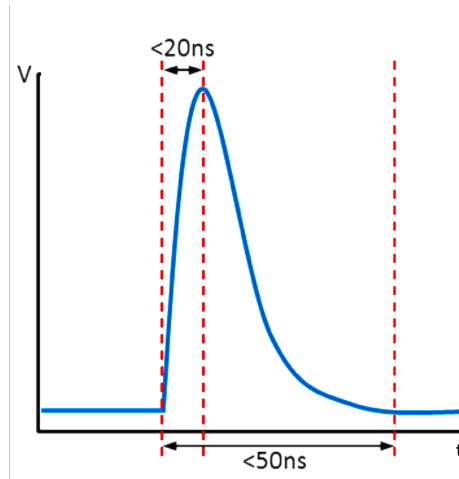


Figure 19: Sketch of the CBC3 pulse shape.

measurement was done scanning the DLL settings of the CBC3 which allows to shift the sampling clock by units of 1 ns. The register controlling the DLL was varied over 3 latency values because the amplifier pulse shape takes about 50 ns to return to the baseline, as shown in Fig. 19.

By measuring the particle detection efficiency at each setting, the amplifier pulse shape can be reconstructed. Figure 20 (a) indicates that the amplifier pulse shape is above threshold for less than 50 ns having a full width at half maximum of ≈ 42 ns as measured from the plot. The peaking time, which is independent of the amount of charge collected, can be determined by analyzing the average cluster width which is maximized when the sampling clock is aligned with the charge peak. Figure 20 (b) shows that the mean cluster width peaks when the phase is at +2 ns, corresponding to a CBC3 chip clock phase shifted by 20 ns with respect to the rising edge of the signal, which, as shown in Figure 20 (a), starts to rise at around -18 ns. This measurement is in agreement with the CBC3 specifications.

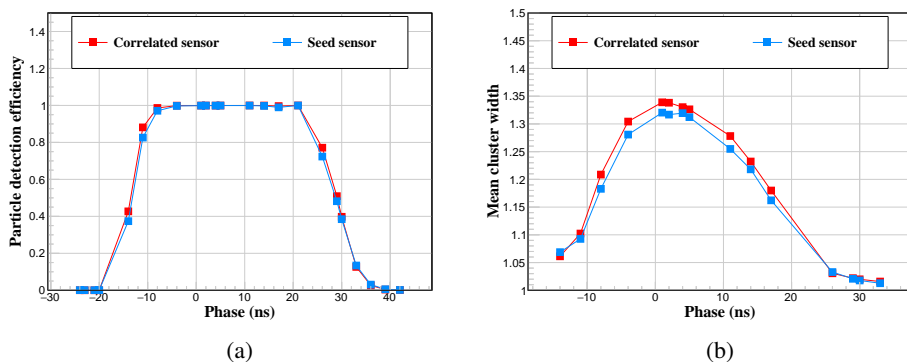


Figure 20: (a) Particle detection efficiency as a function of the clock phase and (b) mean cluster width as a function of the clock phase, for the fully irradiated mini-module.

11.3 Cluster width

While the resolution is the key parameter to assess the module performance, the resolution itself depends on the cluster width. Figure 21 shows distributions of cluster width in the seed sensor for different thresholds (a) and incident angles (b). The two plots show the expected broadening of the clusters for lower thresholds and bigger incident angles (β). In both cases, a long tail of large cluster widths, likely due to delta rays, is visible.

The fraction of clusters of different widths is shown in Fig. 22 as a function of incident angle. For the unirradiated mini-module, at $\beta = 0^\circ$, close to 90% of clusters were single-strip, about 10% were two-strip, and approximately 1% were multi-strip clusters. The fraction of single-strip clusters decreases with increasing incident angle. At around $\beta = 12^\circ$, the fractions of one and two-strip clusters is approximately equal. Two-strip clusters dominate at higher angles, reaching about 75% at 18° . A similar behavior is also observed for the half irradiated mini-module where the crossing point between single-strip and two-strip clusters happens at around $\beta = 12^\circ$, while for the fully irradiated mini-module single-strip and double-strip clusters are still almost equally split at $\beta = 20^\circ$. These plots also show that, when the mini-module is irradiated, the fraction of two-strip clusters increases significantly at $\beta = 0^\circ$ with respect to the unirradiated detector. It should be noted that, in all runs, the fraction of clusters with width three and four, which are dominated by delta rays, do not show a strong dependence on the incident angle. All observations are in agreement with prior measurements in the literature [7]. Figure 23 compares the cluster width for the unirradiated, half irradiated, and fully irradiated mini-module.

11.4 Resolution

In order to assess the expected reconstruction performance throughout the detector lifetime, the detector resolution has been studied for different irradiation fluences. The resolution for clusters of width one is extracted from the fit to their residual distribution. The function used for the fit is a constant linear function convolved with a Gaussian function and the resolution is the sigma of the constant linear function. The function used to fit the residual distribution for clusters of

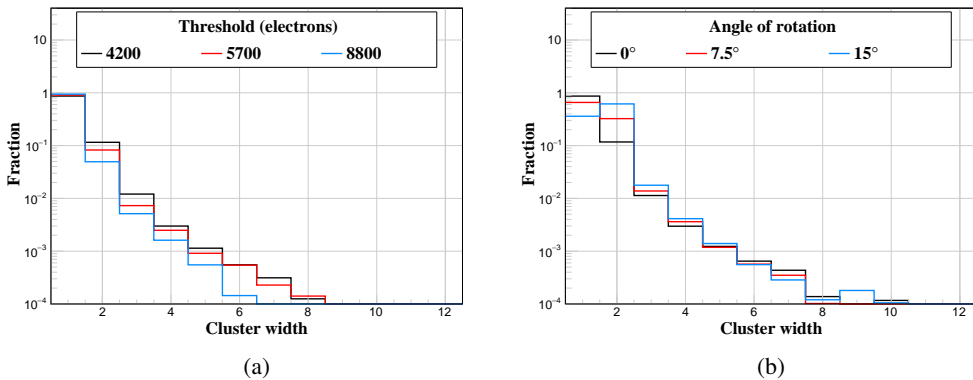


Figure 21: Cluster width for selected values of V_{CTH} (a) and incident angle (b) for the unirradiated mini-module.

width two is a Gaussian function with an offset. The resolution for clusters of width two is the sigma of the Gaussian component of the fit. The residuals are defined, both for clusters and stubs, as the difference between the projected track and the reconstructed position on the sensor. All measurements presented in this paragraph have been done using the standard threshold of 4200 electrons. Figure 24 shows the seed and correlated sensor residual distributions for the unirradiated (a), (c) and the fully irradiated (b), (d) mini-module. The distributions of clusters of width one and width two are shown separately, with their sum overlaid. Wider clusters, which are likely due to delta rays, are not included in the resolution study.

For the unirradiated sensors, Fig. 24 (a) and (c), the residual distributions for clusters of width one show the box like shape that is expected for a $90\ \mu\text{m}$ pitch strip sensor. Smearing at the edges is caused by the telescope resolution and due to tracks near the edges creating two-hit clusters. For the irradiated case the clusters of width one are concentrated in a narrower band around the strip center, which indicates that the charge sharing increases when the sensor is irradiated. As a consequence, only about 10% of the clusters have width two in the unirradiated sensor, as shown previously in Fig. 22, while the percentage increases when the detector is fully irradiated, as can be also seen in

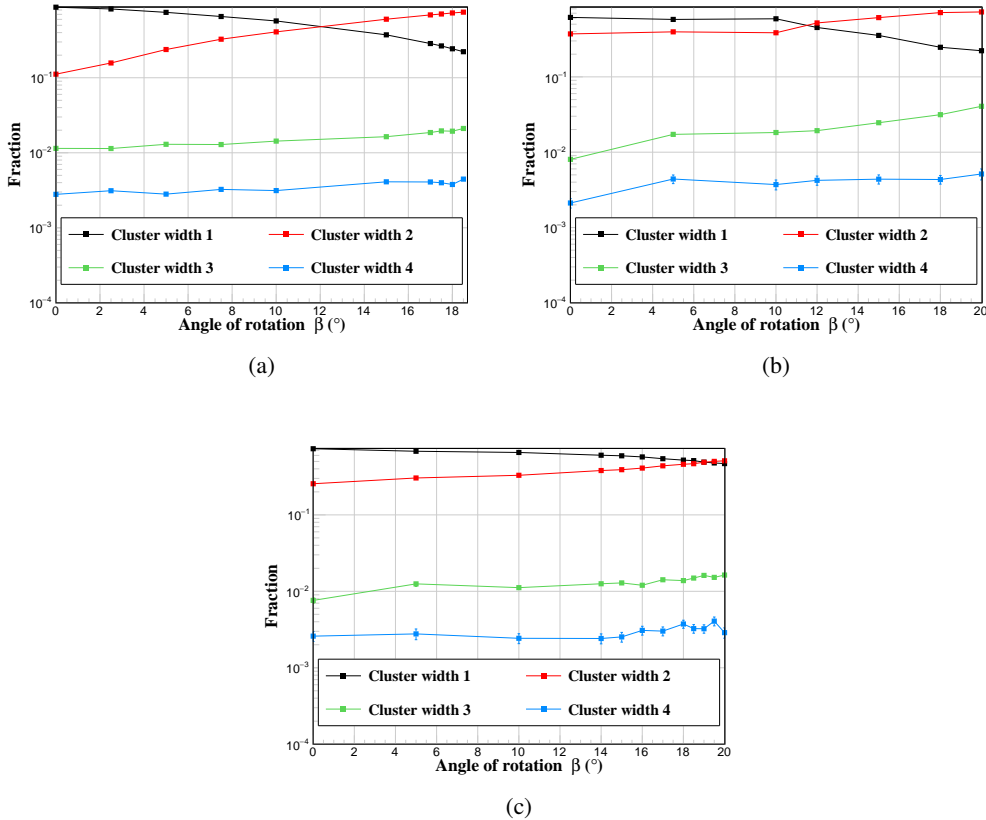


Figure 22: Fraction of clusters with different widths shown as a function of the incident angle. Results are shown for the correlated sensor of the (a) unirradiated , (b) half irradiated and (c) fully irradiated mini-module.

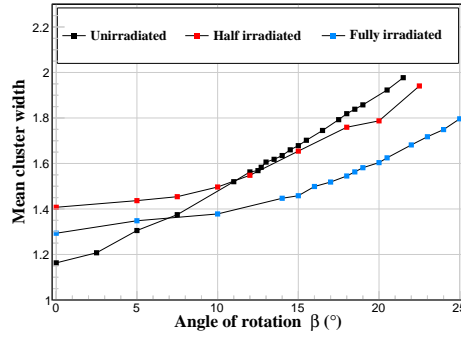


Figure 23: Mean cluster width as a function of incident angle. Results are shown for the correlated sensor of the unirradiated, half irradiated and fully irradiated mini-module.

Figure 24 (b) and Fig. 24 (d).

The resolution of the stubs has been measured for both the unirradiated and the fully irradiated mini-module, with results presented in Fig. 25, and is compared to the values for the clusters in Tab. 2. All values are extracted from the fits and calculated subtracting in quadrature the estimated telescope resolution of $7 \mu\text{m}$. The stub residual distributions show that the CBC3 reconstructs clusters of width one and two very efficiently giving a stub distribution which is very similar to the individual sensor distributions. The detector and stub resolution for clusters of width one and two have also been studied at different incident angles. This is relevant for different parts of the detector along the beamline. Figure 26 and Fig. 27 show how the detector and stub resolution, respectively, varies as a function of incident beam angle for clusters of width one and two. All values are extracted from the fits to the residual distributions and calculated subtracting in quadrature the estimated telescope resolution of $7 \mu\text{m}$. As expected, with increasing incident beam angle, the resolution for clusters of width one improves while for clusters of width two it deteriorates. At any angle the resolution is always between $7 \mu\text{m}$ and $23 \mu\text{m}$ and it does not change significantly between the unirradiated and the irradiated detector. These results confirm that the clusters and stubs can be reconstructed with the expected resolution to allow precise tracking also for trigger purposes even at the end of the detector’s lifetime.

11.5 Charge collection

When the detector is placed orthogonally to the beam, it is possible to measure the charge collected by the sensor by performing a threshold scan and measuring the efficiency using only tracks that point close to the center of the strip, where it is safe to assume that all charge released is collected

Table 2: Resolution summary for normal incident tracks. Width 1 and 2 refer to the cluster width.

Data set	Seed		Correlated		Stub	
	Width 1 (μm)	Width 2 (μm)	Width 1 (μm)	Width 2 (μm)	Width 1 (μm)	Width 2 (μm)
Unirradiated	22.7	7.0	23.0	7.2	22.7	7.0
Fully irradiated	18.0	8.1	18.5	8.4	18.5	8.4

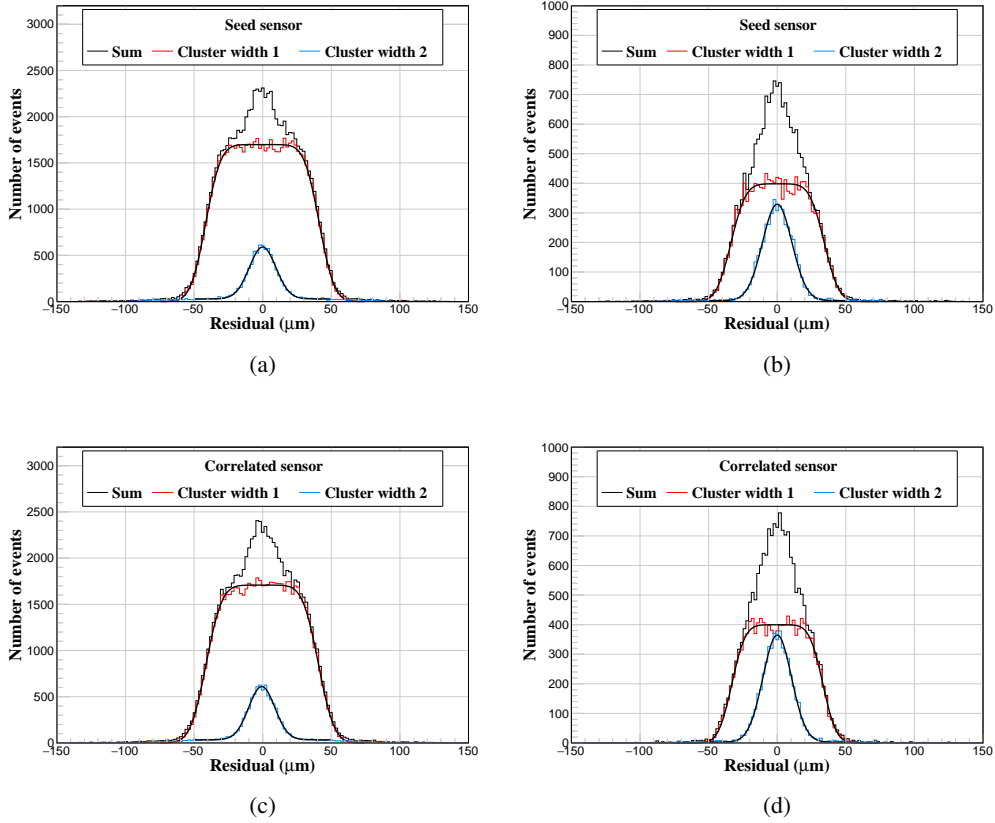


Figure 24: Residual distributions for clusters of width one and two for the unirradiated (a), fully irradiated (b) seed and unirradiated (c), fully irradiated (d) correlated mini-module sensors. The cluster of width one distribution was fitted using a constant linear function convolved with a Gaussian function. The cluster of width two distribution was fitted using a Gaussian function with an offset.

by that strip. A cut of $\pm 5 \mu\text{m}$ around the strip center is used for this analysis. Figure 28 shows the results of these scans from each test beam campaign, with the integral of a Landau function convolved with a Gaussian function superimposed on each scan. Figure 29 shows the Landau function convolved with a Gaussian function obtained by differentiating the fitting functions to the threshold scans. The dashed lines in the figure indicate the returned most probable value (MPV) of the Landau functions.

Figure 30 shows the MPV of each Landau function, as a function of the bias voltage, for the unirradiated, half irradiated and fully irradiated mini-module (no bias scan was performed for the unirradiated mini-module).

The fits to the distributions return 22 003 and 21 985 electrons as MPVs for the correlated and seed sensor, respectively, in case of the unirradiated mini-module, values that are comparable with the expected value of 21 600 electrons for a $300 \mu\text{m}$ thick silicon sensor. The values become 16 496 and 15 789 after the mini-module is fully irradiated.

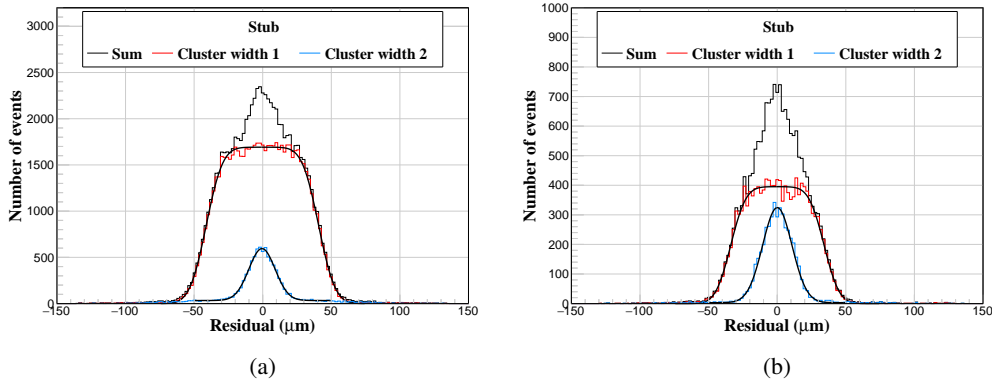


Figure 25: Stub residual distributions for the unirradiated (a) and fully irradiated (b) mini-module. The cluster of width one distribution was fitted using a constant linear function convolved with a Gaussian function. The cluster of width two distribution was fitted using a Gaussian function with an offset.

It is also notable that the two sensors behaved differently from one another after irradiation, exhibiting a slightly different hit efficiency, as can be seen in Fig. 30. This effect is visible after the detector was irradiated at half fluence and at full fluence. The results, nevertheless, show a qualitative agreement with previous charge collection measurements [25].

11.6 Stub reconstruction efficiency

The CBC3 chip version used in the mini-module had the full logic implemented for the stub reconstruction. When hits on both sensors satisfied the requirements to create a stub, the chip was sending it to the FPGA where it was stored to be read out when a trigger was issued. The study of the stub reconstruction efficiency was one of the main goals of this beam test. The same track

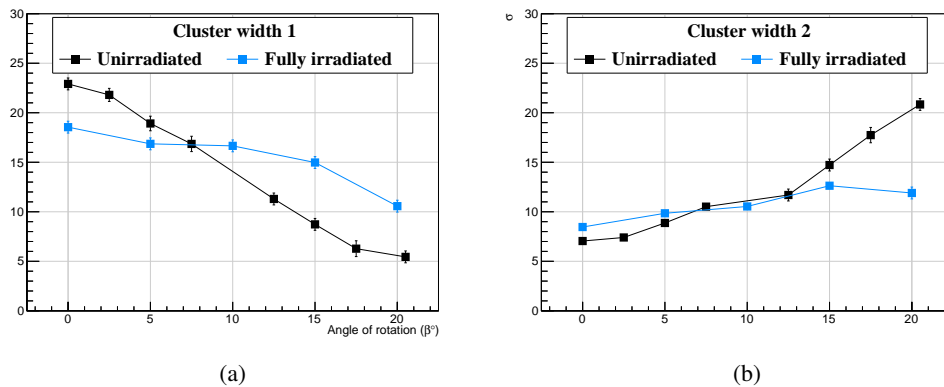


Figure 26: Resolution as a function of incident angle for clusters of width one (a) and width two (b). Results are shown for the correlated sensor of the unirradiated and fully irradiated mini-module.

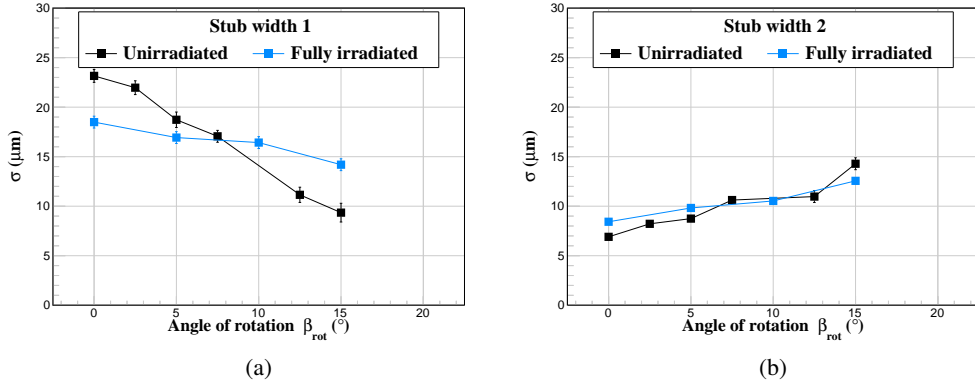


Figure 27: Stub resolution as a function of incident angle for clusters of width one (a) and width two (b). Results are shown for the stubs of the unirradiated and fully irradiated mini-module.

criteria applied for the event selection described in Sec. 11.1 have been used for the analysis of the stub reconstruction efficiency. For the stub efficiency, the denominator is defined as the number of tracks pointing to an active region of the sensor (excluding masked regions and edges, as already described in Sec. 11.1) and there is no offline matching requiring clusters both on the seed and correlated sensors. The numerator includes events in which the mini-module measured at least one stub within a window of $\pm 135 \mu\text{m}$ around the projected impact point.

Figure 31 shows the uniformity of the stub reconstruction efficiency measured across the sensors for the unirradiated (a) and the fully irradiated (b) mini-module. The efficiency is above 99% everywhere along the sensor for the unirradiated mini-module. For the fully irradiated mini-module the efficiency is still around 99%, within the errors.

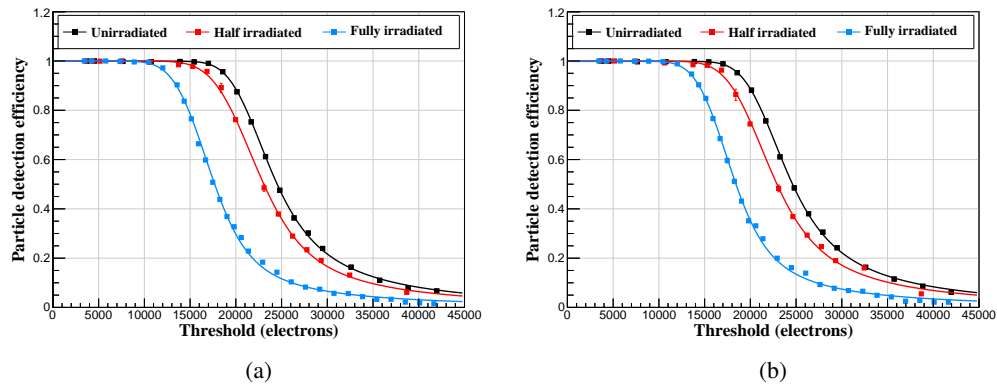


Figure 28: Particle detection efficiency as a function of the threshold, using selected tracks pointing within $\pm 5 \mu\text{m}$ around the strip center, for the (a) seed sensor and (b) correlated sensor. Superimposed on each scan is the best fit performed with the integral of a Landau function convolved with a Gaussian function.

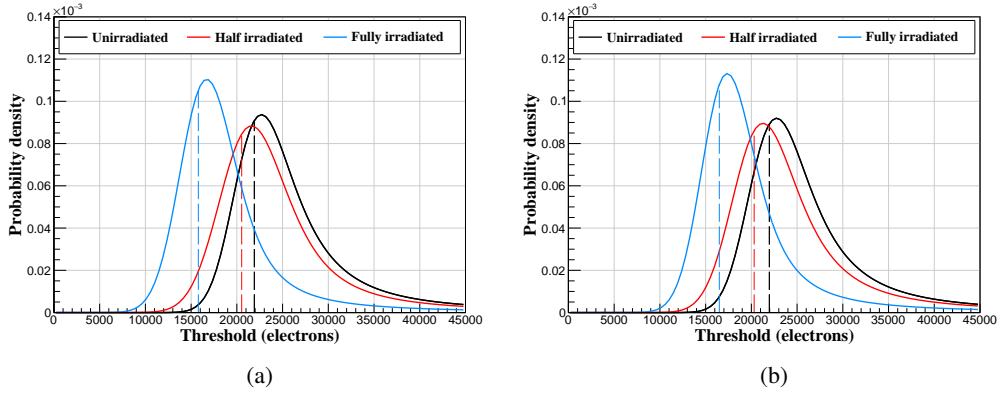


Figure 29: Distributions of the convolution of a Landau function with a Gaussian function, obtained by differentiating the fitting functions to the threshold scans, for the (a) seed sensor and (b) correlated sensor. The dashed lines indicate the Landau functions' most probable value.

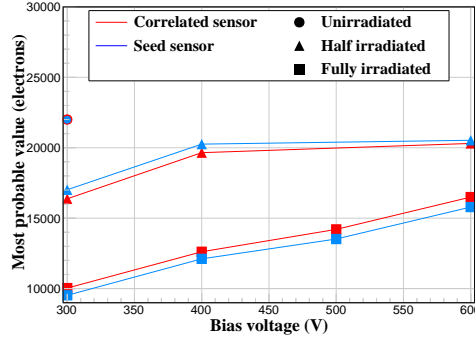


Figure 30: Most probable value of the Landau distribution as a function of the bias voltage for different irradiation fluences.

Since there was no magnetic field during the beam tests, the correlation logic of the CBC3 has been tested by rotating the mini-module, thus emulating the bending of tracks in the CMS magnetic field. For incident angle β , the beam represents a charged particle track with bending radius in the transverse plane r_T . For a module in the tracker with radial position R , $\sin(\beta) = R/(2r_T)$. The bending radius is related to the particle's electric charge (q) and transverse momentum (p_T), for a homogeneous magnetic field of given strength (B), via the relation $r_T = p_T/(qB)$.

For the CMS field strength of $B = 3.8$ T, the relationship between the beam incident angle (β) and the transverse momentum (p_T) of a particle traversing a module at radial position R is given by

$$p_T[\text{GeV}] \approx \frac{0.57 \cdot R[\text{m}]}{\sin \beta}. \quad (11.1)$$

The beam incident angle is related to the stub direction ($\Delta X = X_{\text{seed}} - X_{\text{correlated}}$), in strip units, the strip pitch (p) and the sensor separation (d) via $\tan(\beta) = p\Delta X/d$. The CBC3s on the mini-module were configured to generate stub triggers using a window size of $\pm 4, 5, 6,$ or 7 strips. From

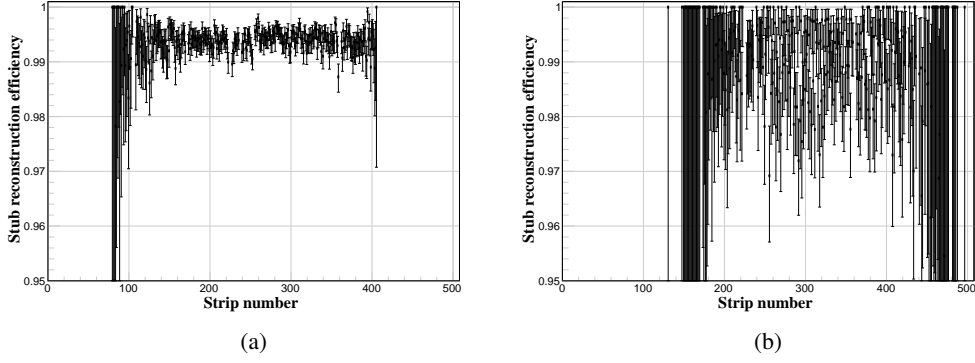


Figure 31: Stub reconstruction efficiency across the sensor for the unirradiated (a) and the fully irradiated (b) mini-module for normal incidence tracks.

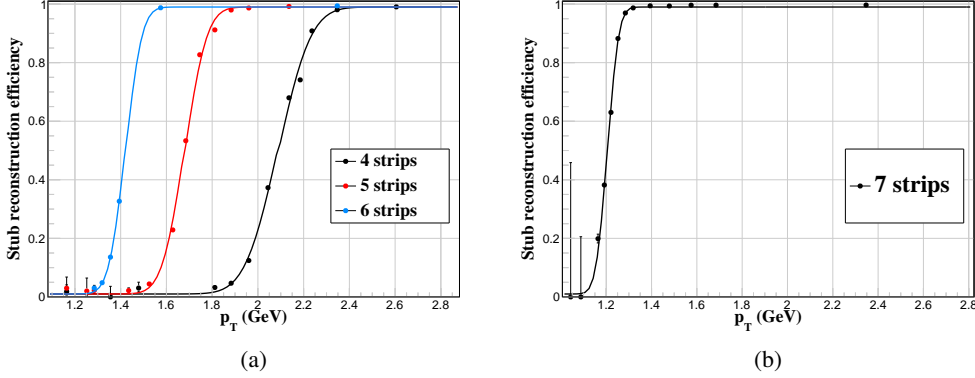


Figure 32: Stub efficiency vs. p_T for the unirradiated (a) and fully irradiated (b) mini-module.

simple geometry, for the known $p = 90 \mu\text{m}$ and the estimated $d = 1.8 \text{ mm} \pm 40 \mu\text{m}$, the efficiency should be constant and high for small angles. The efficiency is expected to start dropping when the incident angle is such that the ΔX is close to the selected window size. If this module were to be placed in the first barrel layer of the CMS tracker at a radius $R = 71.5 \text{ cm}$, using Eq. 11.1, the efficiency is expected to start dropping at $p_T \approx 2.36, 1.86, 1.54, 1.32 \text{ GeV}$, and to reach values around 0 for $p_T \approx 1.86, 1.54, 1.32, 1.16 \text{ GeV}$ corresponding to a window size of 4, 5, 6, 7 strips. Unfortunately a direct comparison using the same window size cut between unirradiated and fully irradiated mini-module stub reconstruction is not possible because of the lack of data. Nevertheless, the measured efficiencies as a function of the rotation angle β are in good agreement with these geometric expectations, as shown in Fig. 32 both for the unirradiated (a) and the fully irradiated (b) mini-module. The efficiencies do not go exactly to zero, likely due to delta rays, stabilizing at around 3% resulting in a rejection efficiency of about 97% for low momentum track hits. By fitting the efficiency curve with an error function, the effective p_T threshold and resolution can be extracted. The effective p_T threshold is defined as the value of p_T for which the efficiency is 50%.

For a window size of 5 strips, the effective p_T is 1.68 GeV with a resolution of 6.5%, defined as the ratio of the sigma of the error function (0.11 GeV) to the p_T value at 50%. The resolution calculated for the irradiated mini-module for a window of 7 strips is 4.6%, with a sigma of 0.055 GeV and a p_T value at 50% of 1.2 GeV.

The efficiency plateau for the unirradiated and fully irradiated module is above 99%. The high plateau efficiencies with sharp turn-on demonstrate that the module can reject hits at the radial distance from the interaction point of $R = 71.5$ cm efficiently.

12 Conclusions

The future CMS Outer Tracker planned for the HL-LHC must provide information about tracks of high transverse momentum to the first level trigger. The main building block of the new tracker will be the so-called p_T -module, equipped with two radiation-tolerant silicon sensors separated by a few millimeters and front-end ASICs that correlate hits on each sensor to reconstruct segments of tracks, called stubs. A fully functional mini-module, using the CMS binary chip version 3.0 for readout and equipped with two 300 μm n-in-p strip sensors, has been analysed in a test beam before and after being irradiated with neutrons. After commissioning, the performance was found to be in agreement with expectations. The particle detection efficiency is close to 100% for the unirradiated mini-module and remains above 99% when the module is irradiated to a fluence that is even higher than the maximum fluence expected during the lifetime of the module when running in CMS, assuming that the HL-LHC upgrade will deliver 4000 fb^{-1} of proton-proton collisions. The cluster width was in good agreement with geometric predictions, and the fraction of very broad clusters was below 1%. The majority of clusters are of width one or two, and the resolution for these clusters behaves as expected. It has also been shown that the charge collected in the fully irradiated mini-module is consistent with the values found in literature. Finally, by emulating the p_T dependent track bending in the magnetic field via a rotation of the mini-module, it has been proven that the stub logic works as expected, rejecting 97% of the the undesired low p_T track points while accepting more than 99% of high p_T track points. For example, it has been shown that particles with momentum below 1.2 GeV could be rejected with a resolution of about 0.055 GeV, when the module was irradiated at the highest fluence. Both before and after irradiation the stub reconstruction efficiency was above 99%, for high p_T tracks.

Acknowledgments

We thank the Fermilab accelerator and FTBF personnel for the excellent performance of the accelerator and support of the test beam facility, in particular M. Kiburg, E. Niner, and E. Schmidt. The tracker groups gratefully acknowledge financial support from the following funding agencies: BMWF and FWF (Austria); FNRS and FWO (Belgium); CERN; MSE and CSF (Croatia); Academy of Finland, MEC, and HIP (Finland); CEA and CNRS/IN2P3 (France); BMBF, DFG, and HGF (Germany); GSRT (Greece); NKFI K124850, and Bolyai Fellowship of the Hungarian Academy of Sciences (Hungary); DAE and DST (India); INFN (Italy); PAEC (Pakistan); SEIDI, CPAN, PCTI and FEDER (Spain); Swiss Funding Agencies (Switzerland); MST (Taipei); STFC (United Kingdom); DOE and NSF (U.S.A.). This project has received funding from the European

Union’s Horizon 2020 research and innovation programme under the Marie Skłodowska-Curie grant agreement No 884104 (PSI-FELLOW-III-3i). Individuals have received support from HFRI (Greece).

This document was prepared using the resources of the Fermi National Accelerator Laboratory (Fermilab), a U.S. Department of Energy, Office of Science, HEP User Facility. Fermilab is managed by Fermi Research Alliance, LLC (FRA), acting under Contract No. DE-AC02-07CH11359.

References

- [1] G. Apollinari, I. Béjar Alonso, O. Brüning, P. Fessia, M. Lamont, L. Rossi, and L. Tavian. High-Luminosity Large Hadron Collider (HL-LHC): Technical Design Report V. 0.1. 4/2017, 2017.
- [2] S. Chatrchyan et al. The CMS Experiment at the CERN LHC. *JINST*, 3:S08004, 2008.
- [3] Armen Tumasyan et al. The Phase-2 Upgrade of the CMS Tracker. Technical Report CERN-LHCC-2017-009, CMS-TDR-014, 2017.
- [4] Davide Ceresa, A. Marchioro, K. Kloukinas, J. Kaplon, W. Bialas, V. Re, G. Traversi, L. Gaioni, and L. Ratti. Macro Pixel ASIC (MPA): the readout ASIC for the pixel-strip (PS) module of the CMS outer tracker at HL-LHC. *JINST*, 9:C11012, 2014.
- [5] Alessandro Caratelli, Davide Ceresa, Jan Kaplon, Kostas Kloukinas, Yusuf Leblebici, Jan Murdzek, and Simone Scarfi. Short-Strip ASIC (SSA): A 65nm silicon-strip readout ASIC for the Pixel-Strip (PS) module of the CMS Outer Tracker detector upgrade at HL-LHC. *PoS*, TWEPP-17:031, 2018.
- [6] Mark L. Prydderch et al. CBC3: a CMS microstrip readout ASIC with logic for track-trigger modules at HL-LHC. *PoS*, TWEPP-17:001, 2018.
- [7] W. Adam et al. Test beam demonstration of silicon microstrip modules with transverse momentum discrimination for the future CMS tracking detector. *JINST*, 13:P03003, 2018.
- [8] G. Hall et al. CBC2: A CMS microstrip readout ASIC with logic for track-trigger modules at HL-LHC. *Nucl. Instrum. Meth. A*, 765:214–218, 2014.
- [9] Infineon, 2022.
- [10] T. Bergauer, U. Bartl, D. Blöch, M. Döcke, M. Dragicevic, J. Hacker, V. Hinger, A. König, E. Pree, and M. Valentan. History, status and prospects of producing silicon sensors for HEP experiments at Infineon Technologies. *Nucl. Instrum. Meth. A*, 924:1–6, 2019.
- [11] Tomasz Gadek, Georges Blanchot, Rafael Gajanec, Alan Honma, and Mark Istvan Kovacs. Front-end hybrids for the strip-strip modules of the CMS Outer Tracker Upgrade. *PoS*, TWEPP2018:019, 2019.
- [12] M. Pesaresi, M. Barros Marin, G. Hall, M. Hansen, G. Iles, A. Rose, F. Vasey, and P. Vichoudis. The FC7 AMC for generic DAQ & control applications in CMS. *JINST*, 10:C03036, 2015.
- [13] C. Ghabrous Larrea, K. Harder, D. Newbold, D. Sankey, A. Rose, A. Thea, and T. Williams. IPbus: a flexible Ethernet-based control system for xTCA hardware. *JINST*, 10:C02019, 2015.
- [14] G. Bauer et al. The CMS Data Acquisition System Software. *J. Phys. Conf. Ser.*, 219:022011, 2010.
- [15] Fermilab. Fermilab off the shelf data acquisition, 2020.
- [16] Fermilab. Fermilab test beam facility, 2019.
- [17] Simon Kwan et al. The Pixel Tracking Telescope at the Fermilab Test Beam Facility. *Nucl. Instrum. Meth.*, A811:162–169, 2016.

- [18] M. Barbero et al. Design and test of the CMS pixel readout chip. *Nucl. Instrum. Meth.*, A517:349–359, 2004.
- [19] Dmitri S. Denisov and Stefan Soldner-Rembold. D0 Run IIB Silicon Detector Upgrade: Technical Design Report. Technical Report FERMILAB-PROPOSAL-0925, FERMILAB-DESIGN-2001-02, 2001.
- [20] V. Re, M. Manghisoni, L. Ratti, J. Hoff, A. Mekkaoui, and R. Yarema. FSSR2, a self-triggered low noise readout chip for silicon strip detectors. *IEEE Trans. Nucl. Sci.*, 53:2470–2476, 2006.
- [21] R. Brun and F. Rademakers. ROOT: An object oriented data analysis framework. *Nucl. Instrum. Meth. A*, 389:81–86, 1997.
- [22] Sarah Seif El Nasr-Storey. Recent developments in the CBC3, a CMS micro-strip readout ASIC for track-trigger modules at the HL-LHC. *Nucl. Instrum. Meth. A*, 936:278–281, 2019.
- [23] Michael Moll. Radiation damage in silicon particle detectors: Microscopic defects and macroscopic properties, PhD thesis, University of Hamburg, 1999.
- [24] Alexander Dierlamm. Selection of the silicon sensor thickness for the Phase-2 upgrade of the CMS Outer Tracker. *JINST*, 16:P11028, 2021.
- [25] W. Adam et al. P-Type Silicon Strip Sensors for the new CMS Tracker at HL-LHC. *JINST*, 12:P06018, 2017.

The Tracker Group of the CMS Collaboration

Institut für Hochenergiephysik, Wien, Austria

W. Adam, T. Bergauer, K. Damanakis, M. Dragicevic, R. Frühwirth¹, H. Steininger

Universiteit Antwerpen, Antwerpen, Belgium

W. Beaumont, M.R. Darwish², T. Janssen, T. Kello³, H. Rejeb Sfar, P. Van Mechelen

Vrije Universiteit Brussel, Brussel, Belgium

N. Breugelmans, M. Delcourt, A. De Moor, J. D'Hondt, F. Heyen, S. Lowette, I. Makarenko, D. Muller, A.R. Sahasransu, D. Vannerom, S. Van Putte

Université Libre de Bruxelles, Bruxelles, Belgium

Y. Allard, B. Clerbaux, S. Dansana⁴, G. De Lentdecker, H. Evard, L. Favart, D. Hohov, A. Khalilzadeh, K. Lee, M. Mahdavihorrani, A. Malara, S. Paredes, N. Postiau, F. Robert, L. Thomas, M. Vandenberg, P. Vanlaer, Y. Yang

Université Catholique de Louvain, Louvain-la-Neuve, Belgium

A. Benecke, G. Bruno, F. Bury, C. Caputo, J. De Favereau, C. Delaere, I.S. Donertas, A. Giammanco, K. Jaffel, S. Jain, V. Lemaître, K. Mondal, N. Szilasi, T.T. Tran, S. Wertz

Universidade Estadual Paulista, São Paulo, Brazil

L. Calligaris

Institut Ruđer Bošković, Zagreb, Croatia

V. Brigljević, B. Chitroda, D. Ferencsek, S. Mishra, A. Starodumov, T. Šušaja

Department of Physics, University of Helsinki, Helsinki, Finland

E. Brücken

Helsinki Institute of Physics, Helsinki, Finland

T. Lampén, L. Martikainen, E. Tuominen

Lappeenranta-Lahti University of Technology, Lappeenranta, Finland

A. Karadzhinova-Ferrer, P. Luukka, H. Petrow, T. Tuuva[†]

Université de Strasbourg, CNRS, IPHC UMR 7178, Strasbourg, France

J.-L. Agram⁵, J. Andrea, D. Apparù, D. Bloch, C. Bonnin, J.-M. Brom, E. Chabert, L. Charles, C. Collard, E. Dangelser, S. Falke, U. Goerlach, L. Gross, C. Haas, M. Krauth, N. Ollivier-Henry

Université de Lyon, Université Claude Bernard Lyon 1, CNRS/IN2P3, IP2I Lyon, UMR 5822, Villeurbanne, France

G. Baulieu, A. Bonnevaux, G. Boudoul, L. Caponetto, N. Chanon, D. Contardo, T. Dupasquier, G. Galbit, M. Marchisone, L. Mirabito, B. Nodari, E. Schibler, F. Schirra, M. Vander Donckt, S. Viret

RWTH Aachen University, I. Physikalisches Institut, Aachen, Germany

V. Botta, C. Ebisch, L. Feld, W. Karpinski, K. Klein, M. Lipinski, D. Louis, D. Meuser, I. Özen, A. Pauls, G. Pierschel, N. Röwert, M. Teroerde, M. Wlochal

RWTH Aachen University, III. Physikalisches Institut B, Aachen, Germany

C. Dziwok, G. Fluegge, O. Pooth, A. Stahl, T. Ziemons

Deutsches Elektronen-Synchrotron, Hamburg, Germany

A. Agah, S. Bhattacharya, F. Blekman⁶, A. Campbell, A. Cardini, C. Cheng, S. Consuegra Rodriguez, G. Eckerlin, D. Eckstein, E. Gallo⁶, M. Guthoff, C. Kleinwort, R. Mankel, H. Maser, C. Muhl, A. Mussgiller, A. Nürnberg, Y. Otariid, D. Perez Adan, H. Petersen, D. Rastorguev, O. Reichelt, P. Schütze, L. Sreelatha Pramod, R. Stever, A. Velyka, A. Ventura Barroso, R. Walsh, A. Zuber

University of Hamburg, Hamburg, Germany

A. Albrecht, M. Antonello, H. Biskop, P. Buhmann, P. Connor, E. Garutti, M. Hajheidari⁷, J. Haller, A. Hinzmann, H. Jabusch, G. Kasieczka, R. Klanner, V. Kutzner, J. Lange, S. Martens, M. Mrowietz, Y. Nissan, K. Pena, B. Raciti, P. Schleper, J. Schwandt, G. Steinbrück, A. Tews, J. Wellhausen

Institut für Experimentelle Teilchenphysik, KIT, Karlsruhe, Germany

L. Ardila⁸, M. Balzer⁸, T. Barvich, B. Berger, E. Butz, M. Caselle⁸, A. Dierlamm⁸, U. Elincabuk, M. Fuchs⁸, F. Hartmann, U. Husemann, G. Kösker, R. Koppenhöfer, S. Maier, S. Mallows, T. Mehner⁸, Th. Müller, M. Neufeld, O. Sander⁸, I. Shvetsov, H. J. Simonis, P. Steck, L. Stockmeier, B. Topko, F. Wittig

Institute of Nuclear and Particle Physics (INPP), NCSR Demokritos, Aghia Paraskevi, Greece

G. Anagnostou, P. Assiouras, G. Daskalakis, I. Kazas, A. Kyriakis, D. Loukas

Wigner Research Centre for Physics, Budapest, Hungary

T. Balázs, M. Bartók, K. Márton, F. Siklér, V. Veszprémi

National Institute of Science Education and Research, HBNI, Bhubaneswar, India

S. Bahinipati⁹, A.K. Das, P. Mal, A. Nayak¹⁰, D.K. Pattanaik, P. Saha, S.K. Swain

University of Delhi, Delhi, India

A. Bhardwaj, C. Jain, A. Kumar, T. Kumar, K. Ranjan, S. Saumya

Saha Institute of Nuclear Physics, HBNI, Kolkata, India

S. Baradia, S. Dutta, P. Palit, G. Saha, S. Sarkar

Indian Institute of Technology Madras, Madras, India

M. Alibordi, P.K. Behera, S.C. Behera, S. Chatterjee, G. Dash, P. Jana, P. Kalbhor, J. Libby, M. Mohammad, R. Pradhan, P.R. Pujahari, N.R. Saha, K. Samadhan, A. Sharma, A.K. Sikdar, R. Singh, S. Verma, A. Vijay

INFN Sezione di Bari^a, Università di Bari^b, Politecnico di Bari^c, Bari, Italy

P. Cariola^a, D. Creanza^{a,c}, M. de Palma^{a,b}, G. De Robertis^a, A. Di Florio^{a,c}, L. Fiore^a, F. Loddo^a, I. Margjeka^a, M. Mongelli^a, S. My^{a,b}, L. Silvestris^a

INFN Sezione di Catania^a, Università di Catania^b, Catania, Italy

S. Albergo^{a,b}, S. Costa^{a,b}, A. Di Mattia^a, R. Potenza^{a,b}, A. Tricomi^{a,b}, C. Tuve^{a,b}

INFN Sezione di Firenze^a, Università di Firenze^b, Firenze, Italy

G. Barbagli^a, G. Bardelli^{a,b}, M. Brianzi^a, B. Camaiani^{a,b}, A. Cassese^a, R. Ceccarelli^{a,b},

R. Ciaranfi^a, V. Ciulli^{a,b}, C. Civinini^a, R. D'Alessandro^{a,b}, E. Focardi^{a,b}, G. Latino^{a,b}, P. Lenzi^{a,b}, M. Lizzo^{a,b}, M. Meschini^a, S. Paoletti^a, A. Papanastassiou^{a,b}, G. Sguazzoni^a, L. Viliani^a

INFN Sezione di Genova, Genova, Italy

S. Cerchi, F. Ferro, E. Robutti

INFN Sezione di Milano-Bicocca^a, Università di Milano-Bicocca^b, Milano, Italy

F. Brivio^a, M.E. Dinardo^{a,b}, P. Dini^a, S. Gennai^a, L. Guzzi^{a,b}, S. Malvezzi^a, D. Menasce^a, L. Moroni^a, D. Pedrini^a, D. Zuolo^{a,b}

INFN Sezione di Padova^a, Università di Padova^b, Padova, Italy

P. Azzi^a, N. Bacchetta^a, P. Bortignon^{a,11}, D. Bisello^a, T. Dorigo^a, E. Lusiani^a, M. Tosi^{a,b}

INFN Sezione di Pavia^a, Università di Bergamo^b, Bergamo, Università di Pavia^c, Pavia, Italy

L. Gaioni^{a,b}, M. Manghisoni^{a,b}, L. Ratti^{a,c}, V. Re^{a,b}, E. Riceputi^{a,b}, G. Traversi^{a,b}

INFN Sezione di Perugia^a, Università di Perugia^b, CNR-IOM Perugia^c, Perugia, Italy

P. Asenov^{a,c}, G. Baldinelli^{a,b}, F. Bianchi^{a,b}, G.M. Bilei^a, S. Bizzaglia^a, M. Caprai^a, B. Checcucci^a, D. Ciangottini^a, A. Di Chiaro^a, L. Fanò^{a,b}, L. Farnesini^a, M. Ionica^a, M. Magherini^{a,b}, G. Mantovani^{a,b}, V. Mariani^{a,b}, M. Menichelli^a, A. Morozzi^a, F. Moscatelli^{a,c}, D. Passeri^{a,b}, A. Piccinelli^{a,b}, P. Placidi^{a,b}, A. Rossi^{a,b}, A. Santocchia^{a,b}, D. Spiga^a, L. Storchi^a, T. Tedeschi^{a,b}, C. Turrioni^{a,b}

INFN Sezione di Pisa^a, Università di Pisa^b, Scuola Normale Superiore di Pisa^c, Pisa, Italy, Università di Siena^d, Siena, Italy

P. Azzurri^a, G. Bagliesi^a, A. Basti^{a,b}, R. Battacharya^a, R. Beccherle^a, D. Benvenuti^a, L. Bianchini^{a,b}, T. Boccali^a, F. Bosi^a, D. Bruschini^{a,c}, R. Castaldi^a, M.A. Ciocci^{a,b}, V. D'Amante^{a,d}, R. Dell'Orso^a, S. Donato^a, A. Giassi^a, F. Ligabue^{a,c}, G. Magazzù^a, M. Massa^a, E. Mazzone^a, A. Messineo^{a,b}, A. Moggi^a, M. Musich^{a,b}, F. Palla^a, S. Parolia^a, P. Prosperia^a, F. Raffaelli^a, G. Ramirez Sanchez^{a,c}, A. Rizzi^{a,b}, S. Roy Chowdhury^a, T. Sarkar^a, P. Spagnolo^a, R. Tenchini^a, G. Tonelli^{a,b}, A. Venturi^a, P.G. Verdini^a

INFN Sezione di Torino^a, Università di Torino^b, Torino, Italy

N. Bartosik^a, R. Bellan^{a,b}, S. Coli^a, M. Costa^{a,b}, R. Covarelli^{a,b}, G. Dellacasa^a, N. Demaria^a, S. Garbolino^a, S. Garrafa Botta^a, M. Grippo^{a,b}, F. Luongo^{a,b}, A. Mecca^{a,b}, E. Migliore^{a,b}, G. Ortona^a, L. Pacher^{a,b}, F. Rotondo^a, C. Tarricone^{a,b}, A. Vagnerini^{a,b}

National Centre for Physics, Islamabad, Pakistan

A. Ahmad, M.I. Asghar, A. Awais, M.I.M. Awan, M. Saleh

Instituto de Física de Cantabria (IFCA), CSIC-Universidad de Cantabria, Santander, Spain

A. Calderón, J. Duarte Campderros, M. Fernandez, G. Gomez, F.J. Gonzalez Sanchez, R. Jaramillo Echeverria, C. Lasaosa, D. Moya, J. Piedra, A. Ruiz Jimeno, L. Scodellaro, I. Vila, A.L. Virto, J.M. Vizan Garcia

CERN, European Organization for Nuclear Research, Geneva, Switzerland

D. Abbaneo, M. Abbas, I. Ahmed, E. Albert, B. Allongue, J. Almeida, M. Barinoff, J. Batista Lopes, G. Bergamin¹², G. Blanchot, F. Boyer, A. Caratelli, R. Carnesecchi, D. Ceresa, J. Christiansen, J. Daguin, A. Diamantis, M. Dudek, F. Faccio, N. Frank, T. French, D. Golyzniak, J. Kaplon, K. Kloukinas, N. Koss, L. Kottelat, M. Kovacs, J. Lalic, A. La Rosa, P. Lenoir, R. Loos, A. Mar-

chioro, A. Mastronikolis, I. Mateos Dominguez¹³, S. Mersi, S. Michelis, C. Nedergaard, A. Onnela, S. Orfanelli, T. Pakulski, A. Papadopoulos¹⁴, F. Perea Albela, A. Perez, F. Perez Gomez, J.-F. Perrot, P. Petagna, Q. Piazza, G. Robin, S. Scarfi¹⁵, K. Schleidweiler, N. Siegrist, M. Sinani, P. Szidlik, P. Tropea, J. Troska, A. Tsirou, F. Vasey, R. Vrancianu, S. Wlodarczyk, A. Zografos¹⁶

Paul Scherrer Institut, Villigen, Switzerland

W. Bertl[†], T. Bevilacqua¹⁷, L. Caminada¹⁷, A. Ebrahimi, W. Erdmann, R. Horisberger, H.-C. Kaestli, D. Kotlinski, C. Lange, U. Langenegger, B. Meier, M. Missiroli¹⁷, L. Noehte¹⁷, T. Rohe, S. Streuli

Institute for Particle Physics and Astrophysics, ETH Zurich, Zurich, Switzerland

K. Androsoy, M. Backhaus, R. Becker, G. Bonomelli, D. di Calafiori, A. Calandri, A. de Cosa, M. Donega, F. Eble, F. Glessgen, C. Grab, T. Harte, D. Hits, W. Lustermand, J. Niedziela, V. Perovic, M. Reichmann, B. Ristic, U. Roeser, D. Ruini, R. Seidita, J. Sørensen, R. Wallny

Universität Zürich, Zurich, Switzerland

P. Bäertschi, K. Bösigler, F. Canelli, K. Cormier, A. De Wit, M. Huwiler, W. Jin, A. Jofrehei, B. Kilminster, S. Leontsinis, S.P. Liechti, A. Macchiolo, R. Maier, U. Molinatti, I. Neutelings, A. Reimers, P. Robmann, S. Sanchez Cruz, Y. Takahashi, D. Wolf

National Taiwan University (NTU), Taipei, Taiwan

P.-H. Chen, W.-S. Hou, R.-S. Lu

University of Bristol, Bristol, United Kingdom

E. Clement, D. Cussans, J. Goldstein, S. Seif El Nasr-Storey, N. Stylianou, K. Walkingshaw Pass

Rutherford Appleton Laboratory, Didcot, United Kingdom

K. Harder, M.-L. Holmberg, K. Manolopoulos, T. Schuh, I.R. Tomalin

Imperial College, London, United Kingdom

R. Bainbridge, J. Borg, C. Brown, G. Fedi, G. Hall, D. Monk, D. Parker, M. Pesaresi, K. Uchida

Brunel University, Uxbridge, United Kingdom

K. Coldham, J. Cole, M. Ghorbani, A. Khan, P. Kyberd, I.D. Reid

The Catholic University of America, Washington DC, USA

R. Bartek, A. Dominguez, C. Huerta Escamilla, R. Uniyal, A.M. Vargas Hernandez

Brown University, Providence, USA

G. Benelli, X. Coubez, U. Heintz, N. Hinton, J. Hogan¹⁸, A. Honma, A. Korotkov, D. Li, J. Luo, M. Narain, N. Pervan, T. Russell, S. Sagir¹⁹, F. Simpson, E. Spencer, C. Tiley, P. Wagenknecht

University of California, Davis, Davis, USA

E. Cannaert, M. Chertok, J. Conway, G. Haza, D. Hemer, F. Jensen, J. Thomson, W. Wei, T. Welton, R. Yohay²⁰, F. Zhang

University of California, Riverside, Riverside, USA

G. Hanson

University of California, San Diego, La Jolla, USA

S.B. Cooperstein, R. Gerosa, L. Giannini, Y. Gu, S. Krutelyov, B.N. Sathia, V. Sharma, M. Tadel,

E. Vourliotis, A. Yagil

University of California, Santa Barbara - Department of Physics, Santa Barbara, USA

J. Incandela, S. Kyre, P. Masterson

University of Colorado Boulder, Boulder, USA

J.P. Cumalat, W.T. Ford, A. Hassani, G. Karathanasis, F. Marini, C. Savard, N. Schonbeck, K. Stenson, K.A. Ulmer, S.R. Wagner, N. Zipper

Cornell University, Ithaca, USA

J. Alexander, S. Bright-Thonney, X. Chen, D. Cranshaw, A. Duquette, J. Fan, X. Fan, A. Filenius, D. Gadhari, J. Grassi, S. Hogan, P. Kotamnives, S. Lantz, J. Monroy, G. Niendorf, H. Postema, J. Reichert, M. Reid, D. Riley, A. Ryd, K. Smolenski, C. Strohman, J. Thom, P. Wittich, R. Zou

Fermi National Accelerator Laboratory, Batavia, USA

A. Bakshi, D.R. Berry, K. Burkett, D. Butler, A. Canepa, G. Derylo, J. Dickinson, A. Ghosh, H. Gonzalez, S. Grünendahl, L. Horyn, M. Johnson, P. Klabbbers, C.M. Lei, R. Lipton, S. Los, P. Merkel, S. Nahn, F. Ravera, L. Ristori, R. Rivera, L. Spiegel, L. Uplegger, E. Voirin, I. Zoi

University of Illinois at Chicago (UIC), Chicago, USA

S. Dittmer, R. Escobar Franco, A. Evdokimov, O. Evdokimov, C.E. Gerber, M. Hackworth, D.J. Hoffman, C. Mills, B. Ozek, T. Roy, S. Rudrabhatla, J. Yoo

The University of Iowa, Iowa City, USA

M. Alhusseini, T. Bruner, M. Haag, M. Herrmann, J. Nachtman, Y. Onel, C. Snyder, K. Yi²¹

Johns Hopkins University, Baltimore, USA

J. Davis, A. Gritsan, L. Kang, S. Kyriacou, P. Maksimovic, S. Sekhar, M. Swartz, T. Vami

The University of Kansas, Lawrence, USA

J. Anguiano, A. Bean, D. Grove, R. Salvatico, C. Smith, G. Wilson

Kansas State University, Manhattan, USA

A. Ivanov, A. Kalogeropoulos, G. Reddy, R. Taylor

University of Nebraska-Lincoln, Lincoln, USA

K. Bloom, D.R. Claes, C. Fangmeier, F. Golf, C. Joo, I. Kravchenko, J. Siado

State University of New York at Buffalo, Buffalo, USA

I. Iashvili, A. Kharchilava, D. Nguyen, J. Pekkanen, S. Rappoccio

Boston University, Boston, USA

A. Akpinar, Z. Demiragli, D. Gastler, P. Gkoutoumis, E. Hazen, A. Peck, J. Rohlf

Northeastern University, Boston, USA

J. Li, A. Parker, L. Skinnari

Northwestern University, Evanston, USA

K. Hahn, Y. Liu, S. Noorudhin

The Ohio State University, Columbus, USA

A. Basnet, C.S. Hill, M. Joyce, K. Wei, B. Winer, B. Yates

University of Puerto Rico, Mayaguez, USA

S. Malik

Purdue University, West Lafayette, USA

R. Chawla, S. Das, M. Jones, A. Jung, A. Koshy, M. Liu, G. Negro, J.F. Schulte, J. Thieman

Purdue University Northwest, Hammond, USA

J. Dolen, N. Parashar, A. Pathak

Rice University, Houston, USA

K.M. Ecklund, S. Freed, A. Kumar, T. Nussbaum

University of Rochester, Rochester, USA

R. Demina, J. Dulemba, O. Hindrichs

Rutgers, The State University of New Jersey, Piscataway, USA

Y. Gershtein, E. Halkiadakis, A. Hart, C. Kurup, A. Lath, K. Nash, M. Osherson, S. Schnetzer,
R. Stone

University of Tennessee, Knoxville, USA

D. Ally, S. Fiorendi, J. Harris, T. Holmes, L. Lee, E. Nibigira, S. Spanier

Texas A&M University, College Station, USA

R. Eusebi

Vanderbilt University, Nashville, USA

P. D'Angelo, W. Johns

Wayne State University, Detroit, USA

R. Harr, N. Poudyal²²

†: Deceased

- 1: Also at Vienna University of Technology, Vienna, Austria
- 2: Also at Institute of Basic and Applied Sciences, Faculty of Engineering, Arab Academy for Science, Technology and Maritime Transport, Alexandria, Egypt
- 3: Also at Université Libre de Bruxelles, Bruxelles, Belgium
- 4: Also at Vrije Universiteit Brussel (VUB), Brussel, Belgium
- 5: Also at Université de Haute-Alsace, Mulhouse, France
- 6: Also at University of Hamburg, Hamburg, Germany
- 7: Now at CERN, European Organization for Nuclear Research, Geneva, Switzerland
- 8: Also at Institute for Data Processing and Electronics, KIT, Karlsruhe, Germany
- 9: Also at Indian Institute of Technology, Bhubaneswar, India
- 10: Also at Institute of Physics, HBNI, Bhubaneswar, India
- 11: Also at University of Cagliari, Cagliari, Italy
- 12: Also at Institut Polytechnique de Grenoble, Grenoble, France
- 13: Also at Universidad de Castilla-La-Mancha, Ciudad Real, Spain
- 14: Also at University of Patras, Patras, Greece
- 15: Also at École Polytechnique Fédérale de Lausanne, Lausanne, Switzerland
- 16: Also at National Technical University of Athens, Athens, Greece
- 17: Also at Universität Zürich, Zurich, Switzerland
- 18: Now at Bethel University, St. Paul, Minnesota, USA
- 19: Now at Karamanoglu Mehmetbey University, Karaman, Turkey
- 20: Now at Florida State University, Tallahassee, USA
- 21: Also at Nanjing Normal University, Nanjing, China
- 22: Now at University of South Dakota, Vermillion, USA